nature COMMUNICATIONS

ARTICLE

Received 28 Dec 2013 | Accepted 25 Jul 2014 | Published 25 Sep 2014

DOI: 10.1038/ncomms5806

Sphingosine-1-phosphate promotes expansion of cancer stem cells via S1PR3 by a ligand-independent Notch activation

Naoya Hirata[1], Shigeru Yamada[1], Takuji Shoda[2], Masaaki Kurihara[2], Yuko Sekino[1] & Yasunari Kanda[1]

Many tumours originate from cancer stem cells (CSCs), which is a small population of cells that display stem cell properties. However, the molecular mechanisms that regulate CSC frequency remain poorly understood. Here, using microarray screening in aldehyde dehydrogenase (ALDH)-positive CSC model, we identify a fundamental role for a lipid mediator sphingosine-1-phosphate (S1P) in CSC expansion. Stimulation with S1P enhances ALDH-positive CSCs via S1P receptor 3 (S1PR3) and subsequent Notch activation. CSCs overexpressing sphingosine kinase 1 (SphK1), an S1P-producing enzyme, show increased ability to develop tumours in nude mice, compared with parent cells or CSCs. Tumorigenicity of CSCs overexpressing SphK1 is inhibited by *S1PR3* knockdown or S1PR3 antagonist. Breast cancer patient-derived mammospheres contain SphK1$^+$/ALDH1$^+$ cells or S1PR3$^+$/ALDH1$^+$ cells. Our findings provide new insights into the lipid-mediated regulation of CSCs via Notch signalling, and rationale for targeting S1PR3 in cancer.

[1] Division of Pharmacology, National Institute of Health Sciences, Setagaya-ku, Tokyo 158-8501, Japan. [2] Division of Organic Chemistry, National Institute of Health Sciences, Setagaya-ku, Tokyo 158-8501, Japan. Correspondence and requests for materials should be addressed to Y.K. (email: kanda@nihs.go.jp).

Growing evidence suggests that many types of cancer, including breast, lung and prostate cancer, are initiated from a small population of cancer stem cells (CSCs; also called tumour-initiating cells)[1–8]. This minor population produces the bulk of cancers through continuous self-renewal and differentiation, which contributes to cancer heterogeneity. Therefore, it is essential to elucidate the signalling and regulatory mechanisms that are unique to CSCs, and to design novel therapeutic agents against CSCs.

CSCs have been isolated from diverse tumours and established cell lines, using several methods encompassing cell surface markers, aldehyde dehydrogenase (ALDH) activity, side population (SP) and sphere-forming ability. ALDH assays rely on the fact that the level of ALDH, a detoxifying enzyme responsible for the oxidation of intracellular aldehydes, is higher in stem cells than in differentiated cells[4]. ALDH1 expression is correlated with poor clinical prognosis in various cancers, such as breast, lung and prostate cancer[4–6]. Because CSCs have been considered to have molecular similarities to embryonic and normal adult stem cells, the self-renewal behaviour of CSCs has been reported to be mediated by several signalling pathways, such as Notch, Hedgehog and Wnt[9]. However, the molecular mechanisms that regulate the frequency and maintenance of CSCs via self-renewal signals remain poorly understood.

Autocrine and paracrine signalling plays a key role in maintaining the stem cell state and expansion of stem cells[10]. We therefore speculated that receptors for autocrine/paracrine factors might play a key role in CSC regulation. Using microarray screening in an ALDH-positive cell population of human breast cancer MCF-7 cells, we found that several receptors are upregulated. Among them, on the basis of pathophysiological properties, we focused on S1P receptor 3 (S1PR3), a receptor for a lipid mediator sphingosine-1-phospahate (S1P). S1P is known to exert multiple responses, such as proliferation, survival and cytoskeletal rearrangement, via its G protein-coupled receptor (GPCR) in many cell types[11]. S1P is synthesized from sphingosine by sphingosine kinase (SphK); two isoforms of mammalian SphK (sphingosine kinase 1 (SphK1) and SphK2) have been cloned and characterized[12,13]. In addition, the SphK1/S1P pathway has also been implicated in tumour progression[14,15]. S1P has also been shown to accumulate in the tumour microenvironment[16]. Although lipid mediators in cancer have been studied extensively, the role(s) of SphK1/S1P in CSCs remain unclear.

We demonstrate here that S1P regulates expansion of CSCs in several types of cancer. Our findings suggest that Notch activation is essential for S1P-induced proliferation of CSCs via S1PR3. We show that SphK1 regulates the tumorigenicity of breast CSCs via S1PR3. Using clinical samples, we show that breast cancer patient-derived CSCs contain SphK1$^+$/ALDH1$^+$ cells or S1PR3$^+$/ALDH1$^+$ cells. Thus, these results implicate the S1P signalling pathway as therapeutic targets in CSCs.

Results

S1P is a regulator of CSC population via S1PR3. We used an ALDH assay system to study the signalling pathways that regulate the frequency and maintenance of CSCs. Many cancer cell lines, including oestrogen receptor-positive MCF-7 cells, are known to contain an ALDH-positive cell population[5,6,17,18]. Consistent with a previous report[4], we confirmed that ALDH-positive cell population in MCF-7 cells possessed CSC-like properties, as assessed by expression of stem cell markers, drug resistance and tumorigenicity (Supplementary Fig. 1). Through microarray analysis, we investigated a possible receptor that increases the proportion of the ALDH-positive cell population in MCF-7 cells as a CSC model. We found *S1PR3* as a possible candidate in CSC regulation (Supplementary Data 1). *S1PR3* was highly expressed in the ALDH-positive cell population, a finding confirmed by quantitative polymerase chain reaction (qPCR) assays (Fig. 1a). *S1PR2* expression was lower in the ALDH-positive cell population compared with MCF-7 cells, and other types of *S1PR* are yet to be detected in MCF-7 cells (Supplementary Fig. 2)[19,20]. Stimulation with S1P increased the proportion of ALDH-positive cell population in a dose-dependent manner, with a maximal response observed at 100 nM (Fig. 1b). Similar to S1P, dihydro-S1P, another S1PR3 ligand, also increased the ALDH-positive cell population (Supplementary Fig. 3). Moreover, stimulation with S1P increased the number of SP cells (Fig. 1c), mammosphere-forming efficiency (Fig. 1d), CD44$^+$/CD24$^-$ population (Fig. 1e) and expression of stem cell markers (Fig. 1f). These data indicate that stimulation with S1P leads to an increase in breast CSCs. In contrast, lysophosphatidic acid (LPA), another well-studied lipid mediator, did not increase CSCs in MCF-7 cells. To confirm the involvement of S1PR3, we inhibited S1PR3 using pharmacological antagonists and RNA interference techniques. The effects of S1P were blocked by the S1PR3 antagonist TY52156 (ref. 21). Another antagonist CAY10444, which is structurally different from TY52156, also inhibited the S1P effect. In contrast, the S1PR2 antagonist JTE013 had little effect (Fig. 1g). Experiments using small interfering RNAs (siRNA) confirmed the effects of antagonists (Fig. 1h). In addition, short hairpin RNAs (shRNAs) against *S1PR3* also inhibited the enhancement of mammosphere-forming ability by S1P (Supplementary Fig.4). Similar results with ALDH assay were obtained in triple-negative MDA-MB-231 cells (Supplementary Fig. 5a,b), suggesting that S1P regulates both luminal and triple-negative type of breast CSCs. Furthermore, we examined CSCs from other tumour types to determine whether these effects of S1P are limited to breast cancer cell lines. Similar to MCF-7 cells, stimulation with S1P increased the ALDH-positive cell population in human lung cancer A549 cells, human prostate cancer LNCaP cells, human glioma U251MG cells and human ovarian cancer OVCAR-5 cells (Supplementary Fig. 6a). In addition, TY52156 inhibited the S1P effect in these cell lines. Taken together, these data demonstrate that S1P has an ability to increase the number of CSCs via S1PR3 in several types of cancer.

S1P enhances Notch signalling via S1PR3. Growing evidence suggests many similarities between embryonic stem cells and CSCs[9]; therefore, we focused on Notch, Hedgehog and Wnt as signalling pathway candidates downstream of the S1PR. Stimulation with S1P induced expression of the Notch target gene *Hes1* in MCF-7 cells (Fig. 2a) and ALDH-positive MCF-7 cells (Supplementary Fig. 7a). Moreover, S1P also induced the *Hes1* expression in ALDH-positive A549, LNCaP, U251 and OVCAR-5 cells (Supplementary Fig. 7b). S1P-induced *Hes1* expression was inhibited by S1PR3 antagonists (Fig. 2b). In contrast, the Hedgehog target gene *Gli1*, and Wnt target gene *Dkk1* were not induced. The effect of S1P on ALDH-positive cell population was inhibited by DAPT, an inhibitor of γ-secretase, which has multiple substrates including Notch, not by the Hedgehog inhibitor cyclopamine and the Wnt inhibitor PNU74654 (Fig. 2c; Supplementary Fig. 8). Similar effects of DAPT were obtained in MDA-MB-231 cells (Supplementary Fig. 5d), A549 cells, LNCaP cells, U251 cells and OVCAR-5 cells (Supplementary Fig. 6b). To determine whether S1P has the ability to activate the Notch pathway, we examined cleavage of Notch in MCF-7 cells. Stimulation with S1P produced the Notch intracellular domain (N1ICD) (Fig. 2d) and induced activation of the Notch transcriptional reporter *CSL*-luc (Fig. 2e). Because *Hes1* expression is dependent on NICD/CSL/MAML

complex-mediated gene transcription[22], we verified whether co-activators were involved in CSCs, using dominant-negative (DN) mutants of CSL, which have been reported to have no ability to bind to DNA[23]. DN-CSL inhibited S1P-induced *Hes1* expression and the ALDH-positive cell population (Fig. 2f). Similar results were obtained by DN-MAML, which lacks transcriptional activating domain and inhibits NICD-dependent transcriptional activition[24]. To examine which subtype of Notch was involved in CSCs, we overexpressed each type of NICD. Overexpression of N1ICD increased *Hes1* expression and the ALDH-positive cell population (Fig. 2g). N3ICD also increased the ALDH-positive cell population (Supplementary Fig. 9a), while N2ICD and

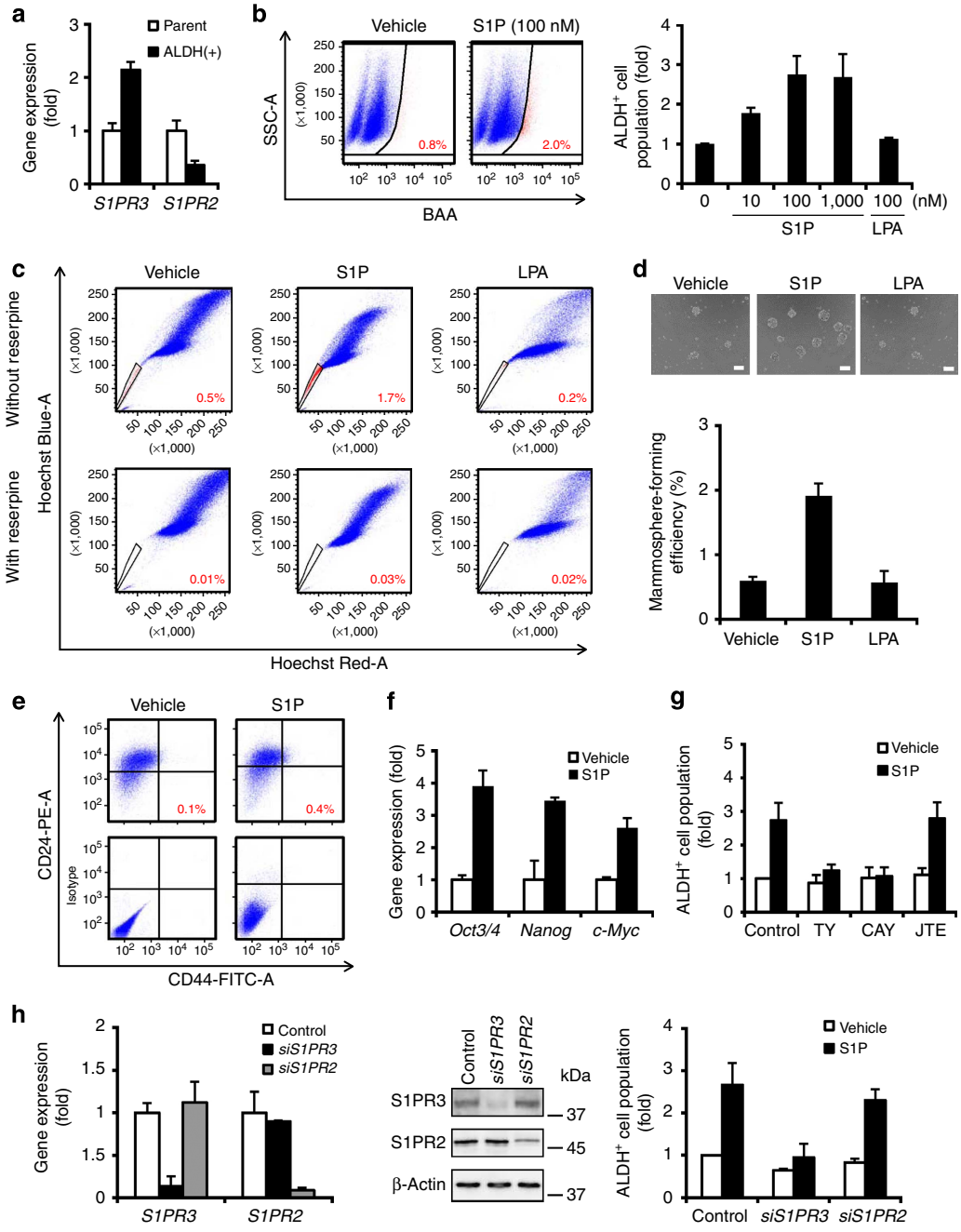

Figure 1 | Role of S1PR3 in the ALDH-positive cell population within the MCF-7 cell line. (**a**) Expression levels of S1PR (*S1PR2* and *S1PR3*) in parental or ALDH-positive MCF-7 cells by qPCR. Data represent mean ± s.d. ($n=3$). (**b**) Representative flow data with ALDH substrate in the presence or absence of S1P (100 nM, 3 days) in MCF-7 cells. Dose-dependent effects of S1P in the proportion of ALDH-positive cell population. Data represent mean ± s.d. ($n=3$). (**c**) Representative flow data of the SP assay with Hoechst 33342 dye alone or in the presence of reserpine (15 μg ml^{-1}). (**d**) Effects of S1P (100 nM) on mammosphere-forming efficiency in MCF-7 cells. The number of mammospheres was microscopically counted and the percentage of mammosphere-forming cells was determined as mammosphere-forming efficiency (%). The scale bar, 100 μm. Data represent mean ± s.d. ($n=3$). (**e**) Effects of S1P (100 nM) on CD44$^+$/CD24$^-$ population in MCF-7 cells. (**f**) Effects of S1P (100 nM) on expression of stem cell markers by qPCR. Data represent mean ± s.d. ($n=3$). (**g**) Effects of S1PR3 antagonists (TY52156, 1 μM; CAY10444, 10 μM) and the S1PR2 antagonist (JTE013, 10 μM) on S1P-induced increase in the ALDH-positive cell population. Data represent mean ± s.d. ($n=3$). (**h**) After transfection with siRNA, expression levels of S1P receptor were examined by qPCR and immunoblotting. Effects of siRNAs against *S1PR3* and *S1PR2* on S1P-induced increase in the ALDH-positive cell population. Data represent mean ± s.d. ($n=3$). Expression levels were normalized to glyceraldehyde 3-phosphate dehydrogenase messenger RNAs.

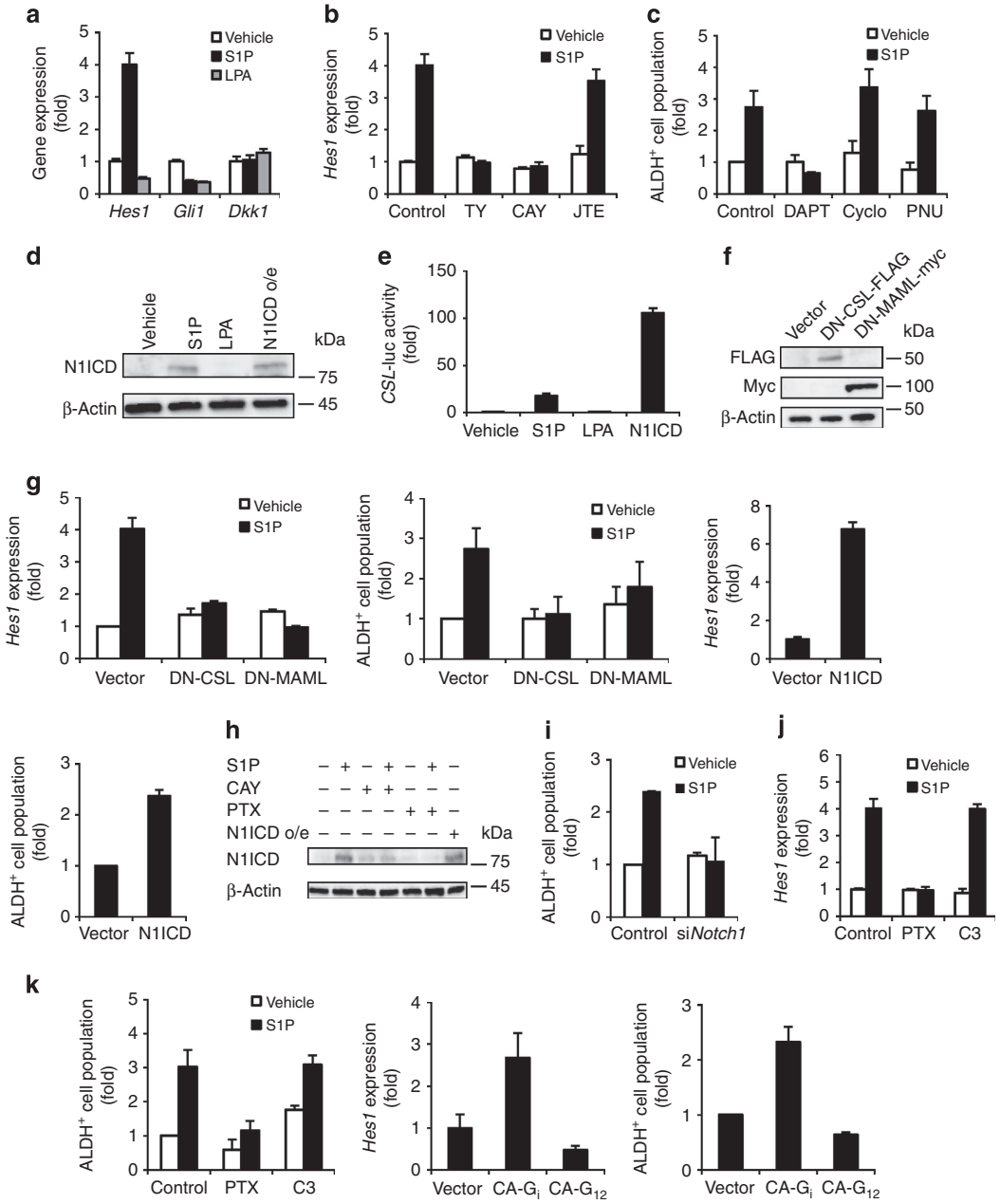

Figure 2 | Role of Notch signalling in ALDH-positive cell population. (**a**) After stimulation with S1P (100 nM) or LPA (100 nM) for 24 h, expression levels of the Notch target gene (*Hes1*), Hedgehog target gene (*Gli1*) and Wnt target gene (*Dkk1*) were quantified in MCF-7 cells using qPCR. Data represent mean ± s.d. ($n=3$). (**b**) Effects of TY52156 (1 μM) or CAY10444 (10 μM) on S1P-induced *Hes1* expression using qPCR. Data represent mean ± s.d. ($n=3$). (**c**) Effects of the Notch inhibitor DAPT (5 μM), the Hedgehog inhibitor cyclopamine (10 μM) or the Wnt inhibitor PNU74654 (10 μM) on S1P-induced increase in the ALDH-positive cell population. Data represent mean ± s.d. ($n=3$). (**d**) Effects of S1P or LPA on N1ICD production by immunoblotting. (**e**) MCF-7 cells transfected with a reporter plasmid encoding CSL-luc were cultured with or without S1P or LPA and were then analysed by luciferase assays. Data represent mean ± s.d. ($n=3$). (**f**) Effects of overexpression of Flag-tagged DN-CSL or myc-tagged DN-MAML on S1P-induced *Hes1* expression and ALDH-positive cell population. Data represent mean ± s.d. ($n=3$). The expression of plasmids was analysed by immunoblotting using tag-specific antibodies. (**g**) Effects of overexpression of N1ICD on *Hes1* expression and ALDH-positive cell population. Data represent mean ± s.d. ($n=3$). (**h**) After pretreatment with PTX (0.1 μg ml^{-1}, 24 h) or CAY10444 (10 μM, 30 min), the cells were stimulated with S1P. N1ICD production was analysed by immunoblotting with N1ICD-specific antibodies. (**i**) Effects of siRNA against *Notch1* on S1P-induced increase in the ALDH-positive cell population. Data represent mean ± s.d. ($n=3$). (**j**) Effects of toxins (PTX, 0.1 μg ml^{-1}; C3 Toxin, 0.1 μg ml^{-1}) on S1P-induced *Hes1* expression and ALDH-positive cell population. Data represent mean ± s.d. ($n=3$). (**k**) Effects of overexpression of CA mutants of G_i or G_{12} on S1P-induced *Hes1* expression and ALDH-positive cell population. Data represent mean ± s.d. ($n=3$). Expression levels were normalized to glyceraldehyde 3-phosphate dehydrogenase messenger RNAs.

N4ICD had little effect. S1P-induced N1ICD production was inhibited by CAY10444 (Fig. 2h); however, S1P did not induce N3ICD production (Supplementary Fig. 9b). To further examine the involvement of Notch in CSC, we performed knockdown experiments using *Notch1* siRNA. Knockdown of *Notch1* inhibited the effect of S1P on ALDH-positive cell population (Fig. 2i; Supplementary Fig. 10). Taken together, these data suggest crosstalk between S1P and Notch1. To confirm the

involvement of S1PR3 in crosstalk, we studied subtype of G proteins coupled to S1PR3. Pertussis toxin (PTX), which inactivates G_i protein, abolished S1P-induced *Hes1* expression and the ALDH-positive cell population, whereas C3 toxin, which inactivates an effector of $G_{12/13}$ Rho, had little effect (Fig. 2j). The effects of toxins were confirmed by overexpression of constitutively active (CA) mutants for G_i, but not by CA-G_{12} (Fig. 2k). These data suggest that G_i mediates S1P-induced Notch activation via S1PR3. Collectively, S1P has an ability to increase the number of CSCs via Notch signalling in several types of cancer.

S1P increases ADAM17 activity without Notch ligands. We further investigated the molecular mechanism of crosstalk between S1P and Notch in MCF-7 cells. Notch is generally activated by binding of Notch ligands to Notch and then cleaved by ADAM17 and γ-secretase[25]. Among Notch ligands (Jagged1, 2 and Delta-like ligand (Dll) 1, 3 and 4), Dll3 is not capable to activate Notch signalling in adjacent cells[26].

To examine whether Notch ligands are required for the S1P effect, we examined the expression level of Notch ligands. S1P did not induce expression levels of Notch ligands (Supplementary Fig. 11a). Knockdown of Notch ligands did not affect S1P-induced *Hes1* expression and ALDH-positive cell population (Fig. 3a,b). In contrast to S1P, knockdown of Notch ligands inhibited hypoxia-mimetic agent desferoxamine-induced *Hes1* expression. In addition, neutralizing antibodies to Jagged1 inhibited *Hes1* induction by soluble Jagged1-Fc, but not S1P-induced *Hes1* expression and ALDH-positive cell population (Supplementary Fig. 11c,d). Taken together, these data suggest that S1P activates Notch signalling in Notch ligand-independent manner.

We next studied cleavage enzymes that are responsible for S1P-induced Notch activation. We found that stimulation with S1P increased ADAM17 activity in MCF-7 cells (Fig. 3c) and ALDH-positive MCF-7 cells (Supplementary Fig. 7c). In addition, S1P also increased γ-secretase activity in MCF-7 cells (Supplementary Fig. 12a). CAY10444 and PTX inhibited S1P-induced ADAM17 activation (Fig. 3d) and γ-secretase activation (Supplementary Fig. 12b). Overexpression of CA-G_i also increased both ADAM17 (Fig. 3e) and γ-secretase activity (Supplementary Fig. 12c). Moreover, we examined whether ADAM17 activation occurred in CSCs. Overexpression of ADAM17 increased N1ICD production, *Hes1* expression and the ALDH-positive cell population (Fig. 3f). Conversely, DN-ADAM17 (E406A; point mutation at metalloprotease domain)[27] inhibited S1P-induced responses (Fig. 3g). Expression of ADAM10 or DN-ADAM10 (E384A; point mutation at metalloprotease domain)[28] had little effect on the CSC signalling pathway. These data suggest that ADAM17 is involved in S1P-induced CSC proliferation.

p38MAPK mediates ADAM17 activation by S1P. We investigated whether the intracellular domain of ADAM17 plays a role in S1P-induced breast CSC proliferation. ADAM17 activity is regulated by phosphorylation-dependent mechanisms[29–31]; therefore, we generated ADAM17 mutants with either Thr735 (p38MAPK consensus motif) or Thr761 (Akt consensus motif) replaced by alanine (Fig. 4a). Consistent with our data above, S1P induced ADAM17 phosphorylation at Thr735 (Fig. 4b). S1P-induced ADAM17 phosphorylation was inhibited by PTX and CAY10444. A mutation at Thr735 decreased ADAM17 phosphorylation through S1P, whereas a mutation at Thr761 had little effect (Fig. 4c). In addition, mutation of Thr735 inhibited S1P-induced ADAM17 activation, *Hes1* expression and the number of ALDH-positive cell population (Fig. 4d). To further confirm the involvement of p38MAPK, we studied the association between p38MAPK and ADAM17. Stimulation with S1P induced a transient phosphorylation of p38MAPK (Supplementary Fig. 13a) and an association between p38MAPK and ADAM17 (Fig. 4e). Mutation of Thr735 abolished this association (Fig. 4f), suggesting that phospho-p38MAPK binds to ADAM17 at Thr735. Treatment with CAY10444 or PTX also inhibited the S1P-induced association between p38MAPK and ADAM17 (Fig. 4g). The p38MAPK inhibitor SB203580 inhibited the S1P-induced responses (Supplementary Fig. 13b–d). Furthermore, SB203580 inhibited the association between p38MAPK and ADAM17 (Supplementary Fig. 13f). In contrast, the PI3-kinase/Akt pathway inhibitor LY294002 had little effect (Supplementary Fig. 13b–e). Taken together, these data suggest that p38MAPK-mediated ADAM17 activation is involved in the S1P-induced CSC phenotype.

SphK1 increases CSCs via S1PR3. S1P is synthesized through SphK-catalyzed phosphorylation of sphingosine[11,14]. We next examined whether SphK is involved in breast CSCs. Consistent with previous reports[32,33], overexpressed SphK1 was localized in the cytosol, and SphK2 was mainly localized to the nucleus (Fig. 5a). Enzyme activities of SphKs were also confirmed (Supplementary Fig. 14). Overexpression of SphK1 increased the number of ALDH-positive cell population in both MCF-7 (Fig. 5b) and MDA-MB-231 cells (Supplementary Fig. 15), whereas SphK2 had little effect. Consistent with the ALDH assay results, ADAM17 activation, N1ICD production and *Hes1* expression were induced by SphK1 but not SphK2 (Fig. 5c). To determine whether intracellular S1P is involved in the SphK1 effect, we tested the effects of the S1PR3 antagonist on SphK1-induced increases in the ALDH-positive cell population. Pretreatment with CAY10444 inhibited SphK1-induced responses (Fig. 5d). *S1PR3* shRNAs also inhibited these SphK1-induced responses (Fig. 5e). Analysis by qPCR confirmed specific suppression of *S1PR3* by these shRNAs (Fig. 5e), and treatment with PTX also produced similar results. Recent studies suggest that the ABC transporter mediates oestrogen-induced S1P secretion in MCF-7 cells[34]. To determine whether the ABC transporter is involved with the SphK1 effect, we used siRNAs and a selective inhibitor to inhibit the transporter. An siRNA against *ABCC1* inhibited SphK1-induced ADAM17 activation, *Hes1* expression and the ALDH-positive cell population (Supplementary Fig. 16a). The ABCC1 inhibitor MK571 also produced similar results (Supplementary Fig. 16b). In contrast, an siRNA against *Spns2*, another S1P transporter[35], had little effects. These data suggest that S1P produced by SphK1 stimulates S1PR3, and leads to an increase in the number of CSCs.

SphK1 accelerates tumour formation of CSCs via S1PR3. Since S1P is easily degraded by S1P lyase or phosphatases, we next studied tumorigenicity using SphK1- or SphK2-overexpressing CSCs in MCF-7 cells. Almost all nude mice injected with SphK1-overexpressing ALDH-positive cells developed tumours within 6 weeks. Tumour formation was inefficient in the mice injected with vector- or SphK2-overexpressing ALDH-positive cells (Fig. 6a,b). Tumour sizes from SphK1-overexpressing ALDH-positive cells were bigger than those from vector- or SphK2-overexpressing ALDH-positive cells (Fig. 6c,d). Histological analysis indicated that tumours derived from the ALDH-positive cells and the SphK1-overexpressing ALDH-positive cells had similar morphologies (Fig. 6e). To examine the proportion of ALDH-positive cells in xenografted tumour samples, we conducted double staining using ALDH assays and human-specific antibodies to TRA-1-85 (Supplementary Fig. 17). The increase in

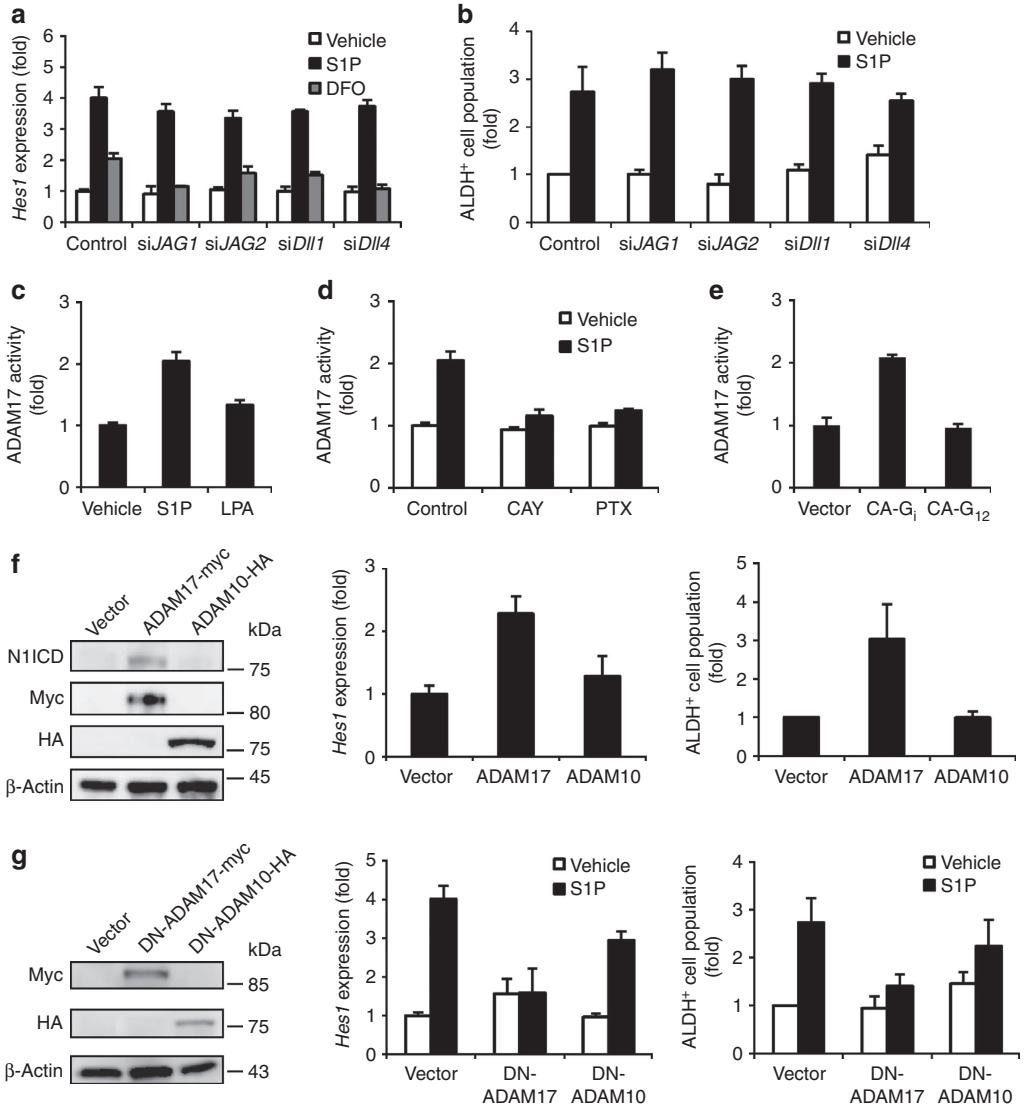

Figure 3 | S1P increases ALDH-positive cell population without Notch ligands. (**a**) Effects of siRNA against *Jagged1*, *Jagged2*, *Dll1* and *Dll4* on desferoxamine- or S1P-induced *Hes1* expression. Data represent mean ± s.d. ($n=3$). (**b**) Effects of siRNA against *Jagged1*, *Jagged2*, *Dll1* and *Dll4* on S1P-induced increase in ALDH-positive cell population. Data represent mean ± s.d. ($n=3$). (**c**) Stimulation with S1P (100 nM, 4 h) increased ADAM17 enzyme activity. Data represent mean ± s.d. ($n=3$). (**d**) S1P-induced ADAM17 activation was inhibited by CAY10444 (10 μM) and PTX (0.1 μg ml^{-1}). Data represent mean ± s.d. ($n=3$). (**e**) ADAM17 activation was induced by the overexpression of CA-G_i, but not by CA-G_{12}. Data represent mean ± s.d. ($n=3$). (**f**) Immunoblotting of N1ICD in ADAM17-myc- and ADAM10-HA-overexpressed MCF-7 cells. The expression of plasmids was confirmed using tag-specific antibody. Effects of overexpression of ADAM17 or ADAM10 on *Hes1* expression in MCF-7 cells. Effects of overexpression of ADAM17 or ADAM10 on ALDH-positive cell population in MCF-7 cells. Data represent mean ± s.d. ($n=3$). (**g**) Effects of DN mutants of ADAM17 or DN-ADAM10 on S1P-induced *Hes1* expression and the ALDH-positive cell population. Data represent mean ± s.d. ($n=3$). Expression levels were normalized to glyceraldehyde 3-phosphate dehydrogenase messenger RNAs.

the proportion of ALDH-positive cells in the tumour paralleled the *in vitro* results, suggesting a stem cell hierarchy (Fig. 6f). Histological analysis and double staining suggest that it is unlikely that the enhanced incidence of tumour formation by expression of SphK1 was due to cell differentiation. To examine whether S1PR3 and ALDH1 were co-expressed in the same cell, we performed double staining of ALDH1 and S1PR3 using xenografted tumour section (Supplementary Fig. 18). The number of ALDH1- and S1PR3 double-positive cells was increased in tumours derived from the SphK1-overexpressing ALDH-positive cells, compared with control and SphK2-overexpressing ALDH-positive cells. In addition, knockdown of *S1PR3* significantly inhibited the tumorigenicity of SphK1-overexpressing ALDH-positive cells, whereas knockdown of *S1PR2* had little effect (Fig. 6g). Furthermore, chronic administration of the S1PR3 antagonist TY52156 significantly inhibited the tumorigenicity of SphK1-overexpressing ALDH-positive cells (Fig. 6h). Taken together, both *in vitro* and *in vivo* results suggest that enhanced expression of SphK1 accelerated tumour formation of CSCs via S1PR3.

Patient-derived CSCs contain SphK1$^+$/ALDH1$^+$ cells. We further extended our observations to primary cell culture. To examine *S1PR3* expression level in breast CSCs, we performed qPCR using secondary mammospheres from patient-derived tumour[8] (Supplementary Table 1). Similar to MCF-7 cells, *S1PR3* was highly expressed in ALDH-positive cells derived from breast cancer patient (Fig. 7a). In addition, we evaluated whether there

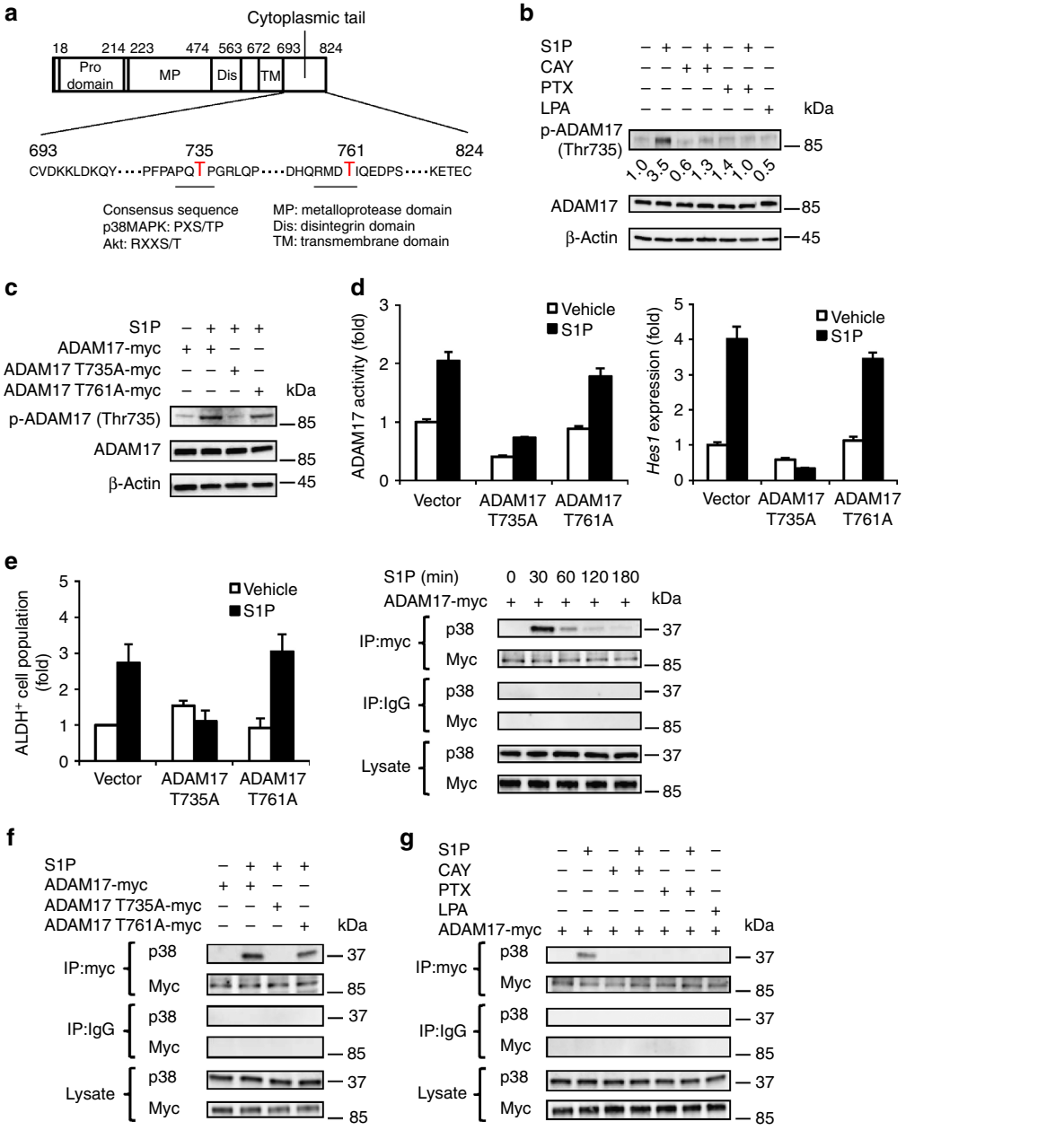

Figure 4 | S1P-induced ADAM17 activation via p38MAPK. (**a**) A schematic of the ADAM17 cytoplasmic domain mutants. (**b**) S1P-induced phosphorylation of ADAM17 at Thr735 was analysed by immunoblotting with a phospho-ADAM17 (Thr735)-specific antibody. (**c**) MCF-7 cells were transfected with ADAM17-T735A-myc or ADAM17-T761A-myc mutants and were then immunoblotted with phospho-ADAM17 (Thr735)-specific antibodies. (**d**) Effects of ADAM17-T735A and ADAM17-T761A mutants on S1P-induced ADAM17 activation, *Hes1* expression and ALDH-positive cell population. Expression levels were normalized to glyceraldehyde 3-phosphate dehydrogenase messenger RNAs. Data represent mean ± s.d. ($n = 3$). (**e**) MCF-7 cells transfected with myc-tagged ADAM17 were either treated or untreated with S1P (100 nM) for the indicated times. The cells were then lysed and subjected immunoprecipitation with myc-specific antibodies, followed by p38MAPK-specific immunoblotting. (**f**) MCF-7 cells were transfected with myc-tagged ADAM17-T735A or T761A and stimulated with S1P (100 nM) for 30 min. The cells were then lysed and subjected to immunoprecipitation with myc-specific antibodies, followed by p38MAPK-specific immunoblotting. (**g**) MCF-7 cells transfected with myc-tagged ADAM17 were treated with S1P (100 nM) or LPA (100 nM) for 30 min in the presence or absence of CAY10444 (10 μM) or PTX (0.1 μg ml^{-1}). The cells were lysed and subjected to immunoprecipitation with myc-specific antibodies, followed by p38MAPK-specific immunoblotting.

were co-expressions of SphK1/ALDH1 or S1PR3/ALDH1 in breast CSCs by immunochemistry. Double staining demonstrated that these patient samples contained SphK1- and ALDH1 double-positive cells or S1PR3- and ALDH1 double-positive cells (Fig. 7b,c). We further evaluated whether SphK1, ADAM17 and N1ICD were co-expressed in the same cell. As a result, patient-derived tumour cells contained triple-positive cells (Fig. 7d). These data suggest that SphK1/S1PR3/Notch signalling is present in CSCs derived from breast cancer patient.

Discussion

In the present study, we used ALDH assays to identify regulators in CSCs, and determined that S1P/S1PR3 signalling and

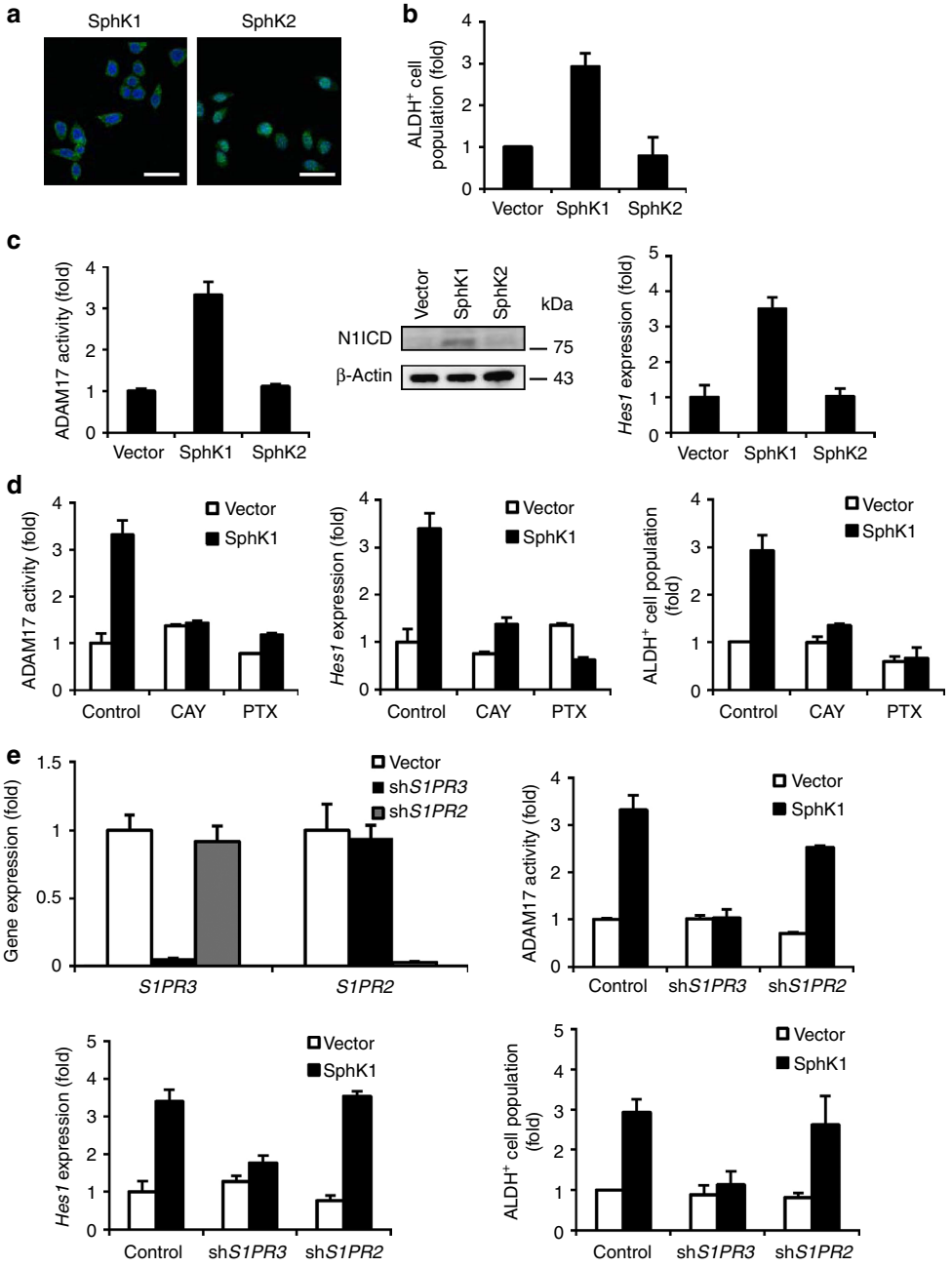

Figure 5 | Role of SphK1 in ALDH-positive cell population. (**a**) Expression of SphK in MCF-7 cells. Plasmid vectors encoding FLAG-tagged SphK1, or HA-tagged SphK2 were transfected into MCF-7 cells before SphK protein levels in cells were analysed by immunostaining. The scale bar indicates 20 μm. (**b**) Effects of SphK1 and SphK2 on the ALDH-positive cell population. Data represent mean ± s.d. ($n=3$). (**c**) Effects of SphK1 and SphK2 on ADAM17 activity, NICD production, and *Hes1* expression. Data represent mean ± s.d. ($n=3$). (**d**) Effects of CAY10444 (10 μM) and PTX (0.1 μg ml^{-1}) on the SphK1-induced ADAM17 activity, *Hes1* expression and ALDH-positive cell population. Data represent mean ± s.d. ($n=3$). (**e**) Expression level of S1P receptor in shRNA-transduced MCF-7 cells. Effects of shRNAs against *S1PR3* and *S1PR2* on the SphK1-induced ADAM17 activity, *Hes1* expression and ALDH-positive cell population. Data represent mean ± s.d. ($n=3$). Expression levels were normalized to glyceraldehyde 3-phosphate dehydrogenase messenger RNAs.

subsequent Notch activation resulted in an increase in the CSCs in several types of cancer (Fig. 8). S1PR3 antagonist inhibited the tumorigenicity of SphK1-overexpressed breast CSCs. Furthermore, breast cancer patient-derived CSCs contained SphK1$^+$/ALDH1$^+$ cells or S1PR3$^+$/ALDH1$^+$ cells. The findings presented here broaden our understanding of the role of lipids in CSC biology, and have significant clinical implications.

We found that S1P has the ability to induce proliferation of several types of CSCs, as stimulation with S1P activates Notch signalling, a key stem cell pathway. As such, S1P might have various roles in stem/progenitor cells. Indeed, S1P has been shown to maintain self-renewal of human embryonic stem cells in cooperation with platelet-derived growth factor[36]. Human-induced pluripotent stem cells have also been shown to express *S1PR3* messenger RNAs, although their biological effects in induced pluripotent stem cells are yet to be elucidated[37]. We postulate that S1P might have self-renewal properties, and play a key role in stem cell regulation.

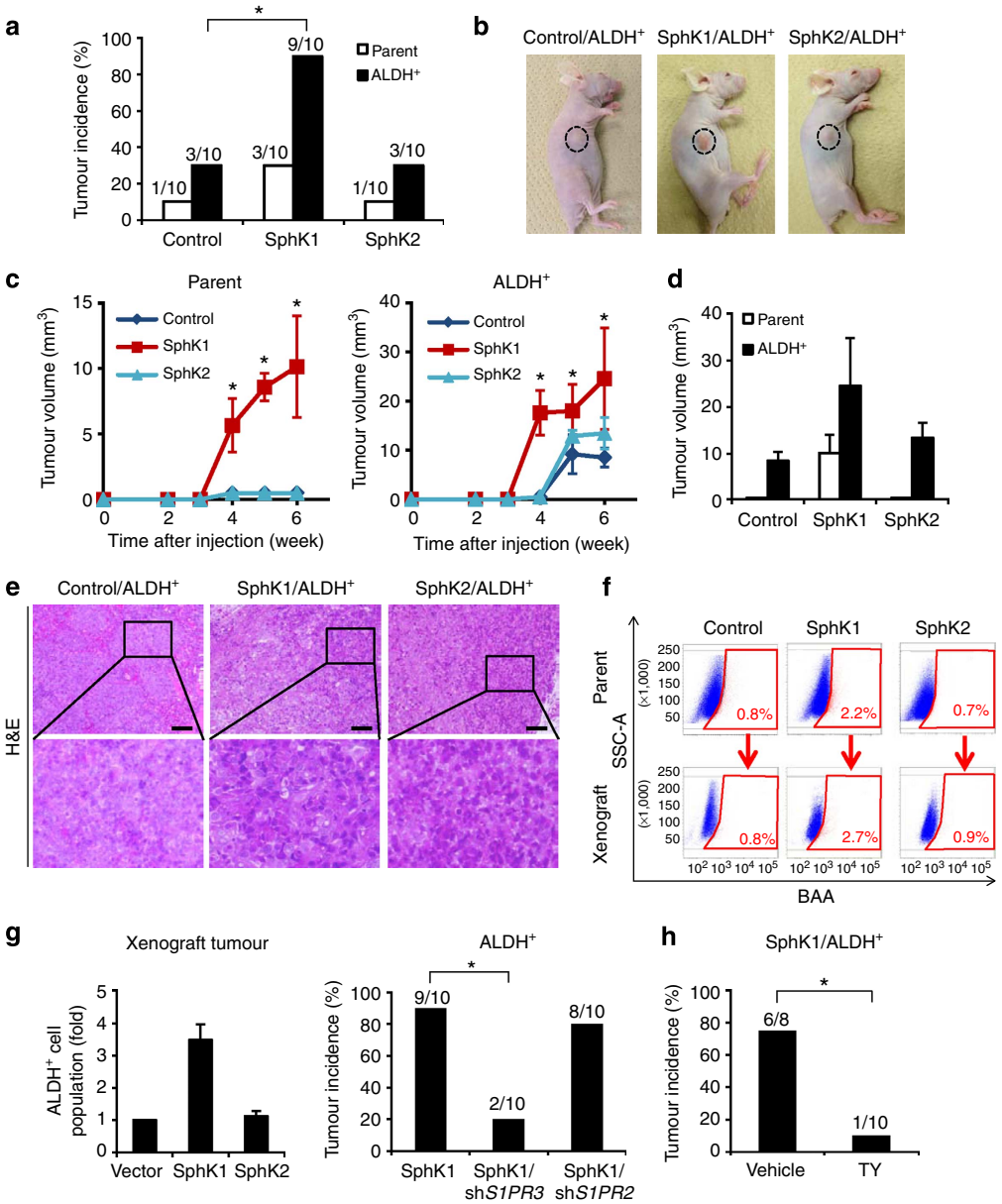

Figure 6 | SphK1 increases CSC-mediated tumour formation in a mouse xenograft model. (**a**) Balb/c nude mice were subcutaneously injected with 1×10^5 vector- or SphK-transfected MCF-7 cells. Tumour formation was indicated by tumours/injections at 6 weeks post injection. The *P* value was calculated using the Fisher's exact test. Bonferroni correction was applied for multiple comparisons. $^*P<0.05$ versus control. (**b**) Photographs of representative nude mice transplanted with ALDH-positive cells, SphK1-overexpressing ALDH-positive cells and SphK2-overexpressing ALDH-positive cells. (**c**) Tumour growth curves in the nude mice injected with parent or ALDH-positive cells. Tumour volume is presented as the mean ± s.d. ($n=10$). Kruskal–Wallis test, followed by the Steel–Dwass was used to determine significance. $^*P<0.05$ versus control. (**d**) Tumour volumes at 6 weeks post injection. Data represent mean ± s.d. ($n=10$). (**e**) Hematoxylin/eosin (H&E)-stained sections of tumour xenografts derived from vector-, SphK1-, and SphK2-overexpressing ALDH-positive cells. Scale bar, 100 μm. (**f**) Representative flow cytometry analysis of ALDH activity in the xenograft tumours derived from vector-, SphK1-, and SphK2-overexpressing ALDH-positive cells. The graph indicates ALDH-positive cell population in xenograft tumours. Data represent mean ± s.d. ($n=3$). ALDH-positive cells were able to regenerate the phenotypic heterogeneity in the xenograft tumours of nude mice. (**g**) Balb/c nude mice were subcutaneously injected with 1×10^5 vector-, *S1PR3*- or *S1PR2*-knockdown cells from SphK1-overexpressing ALDH-positive cells. Tumor formation was indicated by tumours/injections at 6 weeks post injection. The *P* value was calculated using the Fisher's exact test. Bonferroni correction was applied for multiple comparisons. $^*P<0.05$ versus control. (**h**) TY52156 or vehicle was inserted in subcutaneously implanted Alzet osmotic pumps before injection of 1×10^5 SphK1-overexpressing ALDH-positive cells. Tumour formation was indicated by tumours/injections at 6 weeks post injection. The *P* value was calculated using the Fisher's exact test. $^*P<0.05$ versus control.

We also identified S1P-induced Notch activation without Notch ligands. Consistent with our observations, previous studies have shown that ADAM17 mediates ligand-independent Notch activation, while ADAM10 is ligand dependent[38,39]. Another study has shown that soluble form of Jagged1 activates Notch signalling without cell–cell contact[40]. Furthermore, a recent study showed that multiple GPCRs, including the S1PR, resulted in shedding of TGFα via ADAM17 activation in HEK293 cells[41]. Within the S1PR family, S1PR3 has higher intrinsic activity for shedding. These data strongly support a signalling pathway

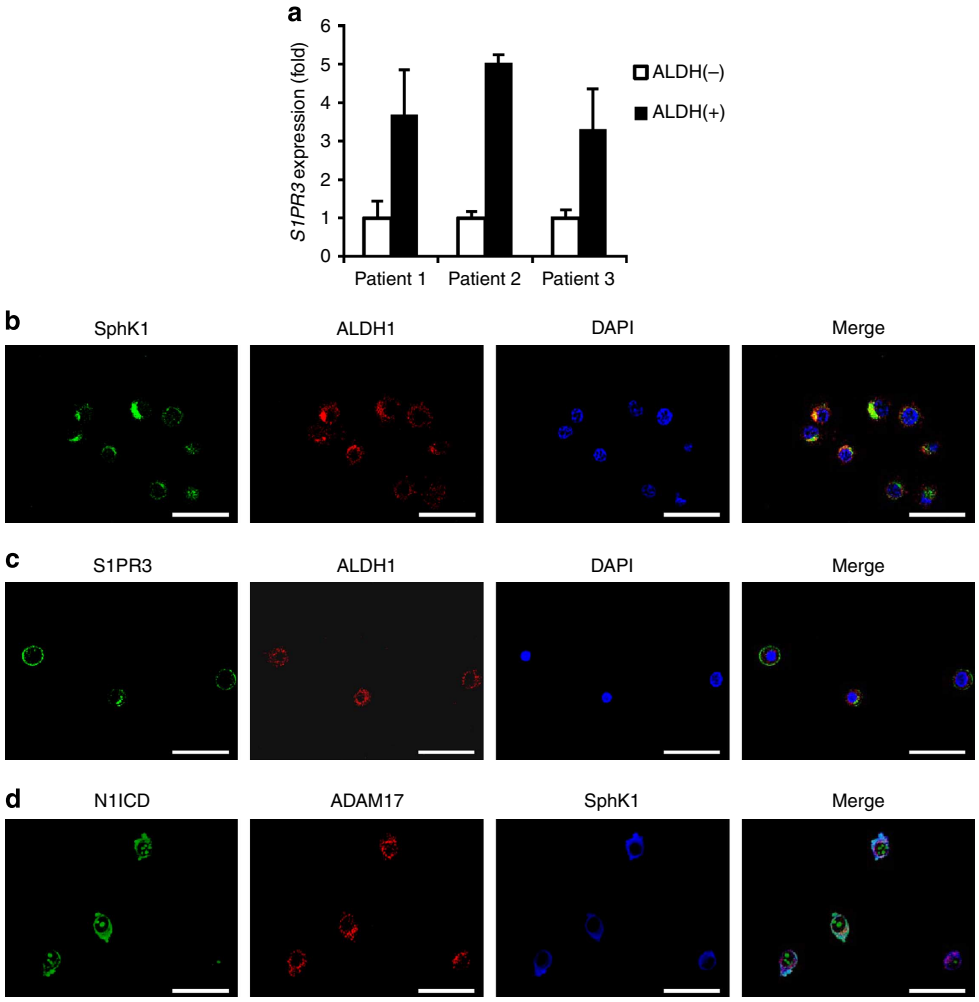

Figure 7 | SphK1-positive CSCs in human breast cancers. (**a**) *S1PR3* expression in the ALDH-negative or ALDH-positive patient-derived cells by qPCR. Expression levels were normalized to glyceraldehyde 3-phosphate dehydrogenase messenger RNAs. Data represent mean ± s.d. ($n = 3$). (**b**) Double immunostaining of SphK1 (green) and ALDH1 (red) in patient-derived tumour cells. Nuclei were counterstained by DAPI (blue). (**c**) Double immunostaining of S1PR3 (green) and ALDH1 (red) in patient-derived tumour cells. Nuclei were counterstained by DAPI (blue). (**d**) Triple immunostaining of N1ICD (green), ADAM17 (red) and SphK1 (blue) in patient-derived tumour cells. Scale bar, 20 μm.

between the S1PR and ADAM17 activation in Notch ligands-independent manner. Further studies should be conducted looking at how the Notch system induces CSC phenotypes in breast cancer.

Our data demonstrate an essential cell autonomous role of Notch1 in breast CSCs expansion. Harrison *et al.*[42] has reported that Notch4 also affects breast CSCs. They performed knockdown of Notch paralog (Notch1 and Notch4) using both $ESA^+/CD44^+/CD24^{low}$ and mammosphere prepared from MCF-7 cells, although Notch ICD overexpression was not examined. Notch1 knockdown reduced only mammosphere population, whereas Notch4 knockdown reduced both $ESA^+/CD44^+/CD24^{low}$ and mammosphere populations (as shown in Figs 3a and 4b). Because Ginestier *et al.*[4] have already reported that two stem-like cell populations defined by ALDH positive and $CD44^+/CD24^-/lin^-$ were not identical, there is a possibility that discrepancy between our present data and Harrison's report is caused by the differences of cell populations used in the experiments. Thus, Notch paralog possibly plays a role in regulation in different stem cell population.

Our clinical samples suggest the crosstalk between Sphk1-S1P-S1PR3 and Notch signalling by co-localization of the components for the crosstalk machinery. Similar observations were obtained using xenografted tumour samples in nude mice. SphK1 has been already shown to be upregulated in patients with breast cancer[43], and its expression correlates with cancer progression and poor prognosis[43–45]. In addition, S1PR3 is the most highly expressed S1PR in breast cancer cells[46]. Thus, our data provide a potential explanation for significance of Sphk1-S1PR3-Notch axis in breast cancer.

Targeting Notch has been expected to facilitate tumour regression[47]. Although several types of Notch inhibitors are quite effective in preclinical models[21,48,49], none of the clinical trials conducted so far has examined effectiveness[50]. This prompts us to encourage efforts to explore alternative/additional approaches for targeting Notch. Our evidence suggests that Notch1 is involved in the S1P-induced CSC phenotype. Because lipid signalling acts upstream of the Notch, S1PR3 could be a promising target for various cancer. Indeed, TY52156 inhibited the tumorigenicity of SphK1-overexpressing breast CSCs (Fig. 6). Although several S1PR antagonists are currently available[14], few have been tested in clinical trials. The feasibility of S1PR3 antagonists in cancer remains to be determined.

In conclusion, the identification of S1P-derived CSC phenotype is required for continuous tumour growth, and points to potential

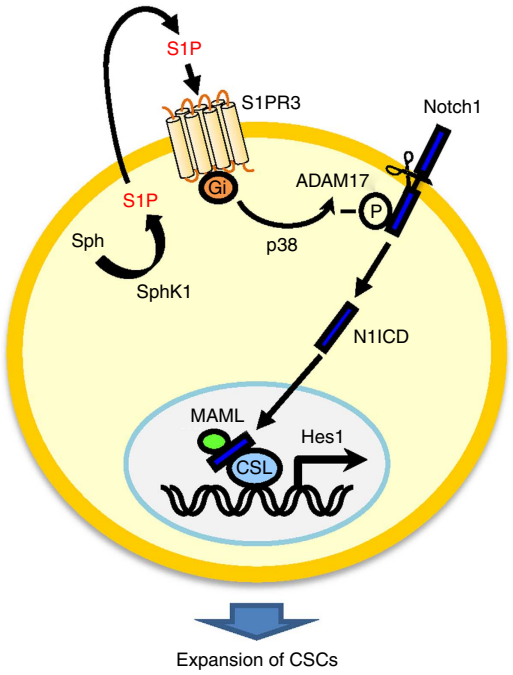

Figure 8 | A working model for the functions of SphK/S1P/S1PR3 in CSC regulation. S1P produced by SphK1 stimulates S1PR3 and subsequently activates Notch signaling in a Notch ligand-independent manner. Activation of S1P signaling pathway leads to expansion of CSCs.

culprits of tumour formation in patients. In the future, it might be possible to establish specific treatments that reduce tumorigenesis by targeting 'stemness' in cancer. Thus, efforts should be made to develop drugs capable of inhibiting CSC self-renewal and expansion by S1PR3.

Methods

Materials. Antibodies to p38MAPK (#9212), phospho-p38MAPK (#9211), Akt (#9272), phospho-Akt (#9271), Notch1 (#4380), N1ICD (#2421) and Notch3 (#2889) were from Cell Signaling Technology. Antibodies to HA (#H6908), FLAG (M2) (#F1804), myc (#C3956), β-actin (#A5441) and ADAM17 (phospho-Thr735) (#SAB4504073) were from Sigma-Aldrich. Antibody to ADAM17 (#AB19027) was from Millipore. Antibody to APC-conjugated TRA-1-85 (#FAB3195A) was from R&D Systems. Antibody to SphK1 (#AP7237c) was from Abgent. Antibody to ALDH1 (#611194), FITC mouse anti-human CD44 (#555478), PE mouse anti-human CD24 (#555428), FITC mouse IgG2b κ isotype control (#555742) and PE mouse IgG2a κ isotype control (#555574) were from BD Biosciences. Antibodies to S1PR2 (#sc-25491), S1PR3 (#sc-30024) and Spns2 (#130102) were from Santa Cruz Biotechnology. Antibody to SphK1 (#ab46719), ADAM17 (#ab57484), activated Notch1 (#ab8925) and ABCC1 (#ab3368) were from Abcam. Antibody to Alexa488-conjugated anti-rabbit IgG (#A11034) and Alexa555-conjugated anti-mouse IgG (#A21424) were from Invitrogen. S1P, dihydro-S1P, DAPT, SB203580, 5-Fluorouracil and doxorubicin were from Enzo Life Sciences. CAY10444, JTE013, MK571, LY294002, cyclopamine were from Cayman Chemicals. LPA was from Avanti Polar Lipids. Jagged1-Fc, Sonic hedgehog and Wnt3a were from R&D Systems. Botulinum C3 enzyme was from Bio Academia. PTX were from Wako Pure Chemical (Osaka, Japan). Hoechst, reserpine, DFO and PNU74654 were from Sigma-Aldrich, while N,N′-bis(4-chlorophenyl)-3,3-dimethyl-2-oxobutanehydrazonamide (TY52156) was synthesized. All other reagents were of analytical grade and obtained from commercial sources.

Cell culture. MCF-7 cells (American Type Culture Collection), MDA-MB-231 cells (American Type Culture Collection), A549 cells (European Collection of Cell Cultures) and LNCaP cells (European Collection of Cell Cultures), U251 cells (Japanese Collection of Research Biosources) were cultured in Dulbecco's modified Eagle's medium (DMEM; Sigma-Aldrich) supplemented with 10% heat-inactivated fetal bovine serum (FBS; Biological Industries), 100 U ml^{-1} penicillin and 100 μg ml^{-1} streptomycin (Gibco BRL). OVCAR-5 cells was cultured in RPMI1640 (Sigma-Aldrich) supplemented with 10% heat-inactivated FBS (Biological Industries), 100 U ml^{-1} penicillin and 100 μg ml^{-1} streptomycin (Gibco BRL).

Plasmid constructs and reporter assays. Plasmids encoding SphK1, SphK2, DN-CSL, DN-MAML, N1ICD, ADAM10 and 12xCSL-luc were kindly provided from Drs Stuart M. Pitson (University of Adelaide), Taro Okada (Kobe University), Aly Karsan (British Columbia Cancer Research Centre), Anthony J. Capobianco (University of Pennsylvania), Spyros Artavanis-Tsakonas (Harvard Medical School), Stefan Lichtenthaler (Ludvig Maximilians University) and Lothar J. Strobl (German Research Center for Environmental Health), respectively. Plasmids encoding N2ICD, N3ICD and N4ICD were kindly provided by Dr Michael J. Hendzel (University of Alberta). Plasmids encoding ADAM17 and DN-ADAM17 were kindly provided by Dr Rik Derynck (University of California, San Francisco). Plasmids encoding CA-G_i and CA-G_{12} were kindly provided by Dr J. Silvio Gutkind (National Institutes of Health). Plasmids encoding the ADAM17 mutants T735A and T761A were generated by QuikChange Site-Directed Mutagenesis (Stratagene) using pRK5-ADAM17-myc. A plasmid encoding the ADAM10 mutant E384A (DN-ADAM10) was generated by QuikChange Site-Directed Mutagenesis using peak-12-ADAM10-HA. Coding DNA sequences were verified by DNA sequencing. Transfections were conducted with FuGENE HD transfection reagent (Promega). Luciferase activity was assayed 24 h after transfection with 12xCSL-luc using the Glo Luciferase Assay Kit (Promega).

Microarray analysis. Total RNAs were isolated by Trizol (Invitrogen) and then purified using an RNeasy Mini Kit (Qiagen). Affymetrix Genome U133A gene chips (Affymetrix) were used to examine gene expression patterns according to the manufacturer's instruction. Genes upregulated more than twofold are shown in Supplementary Data 1.

ALDH assays. The ALDEFLUOR kit (Stem Cell Technologies) was used to detect CSC populations with high ALDH enzyme activity according to the manufacture's instruction[18]. The cells were plated at a density of 3×10^5 cells in 100 mm culture dishes. After serum deprivation for 3 days, cells were suspended at a concentration of 1×10^6 cells ml^{-1} in ALDH assay buffer containing the ALDH substrate BAAA (1 μM) and incubated for 30 min at 37 °C. As a negative control, cells were treated with diethylaminobenzaldehyde (15 μM), a specific ALDH inhibitor. A FACS Aria II cell sorter (BD Biosciences) was used to measure the ALDH-positive cell population.

Mammosphere-forming assays. MCF-7 cells were plated as single cells on ultralow attachment 6-well plates (Corning) at a concentration of 10,000 cells ml^{-1} in serum-free DMEM supplemented with N_2 supplement (Gibco) and 20 ng ml^{-1} basic Fibroblast Growth Factor (R&D Systems). After 4 days, the number of mammospheres was microscopically counted and the percentage of mammosphere-forming cells was determined as mammosphere-forming efficiency (%)[7].

SP assays. Cells were collected and suspended in prewarmed DMEM containing 2% FBS and 2 mM HEPES buffer. Hoechst 33342 dye (Sigma-Aldrich) was then added to a final concentration of 5 μg ml^{-1}, and the mixture was incubated with intermittent shaking for 60 min at 37 °C in the presence or absence of reserpine (15 μg ml^{-1}; Sigma-Aldrich). Cells were then resuspended in ice-cold phosphate-buffered saline (PBS) containing 2% FBS, and analysed with a FACS Aria II cell sorter (BD Biosciences).

CD44$^+$/CD24$^-$ cell population. Cells were resuspended in PBS containing 5% FBS and incubated with FITC mouse anti-human CD44 (#555478, 1:5) and PE mouse anti-human CD24 (#555428, 1:5) for 15 min at 4 °C. FITC mouse IgG2b κ isotype control (#555742, 1:5) and PE mouse IgG2a κ isotype control (#555574, 1:5) were used as negative control. Analysis was performed using a FACS Aria II cell sorter (BD Biosciences).

Cell viability assays. MCF-7 cells and sorted ALDH-positive cells were plated onto 96-well plates at a density of 5,000 cells well^{-1}. After overnight culture, cells were treated with 100 μM 5-Fluorouracil or 10 μM doxorubicin. After 72 h, MTS assays were performed, according to the manufacturer's instruction (Promega).

qPCR assays. Total RNA was isolated from MCF-7 cells using Trizol (Invitrogen), according to the manufacturer's instructions. The qPCR assays were conducted with the aid of a QuantiTect SYBR Green RT-PCR Kit (Qiagen) and an ABI PRISM 7900HT sequence detection system (Applied Biosystems). The relative changes in transcript levels for each sample were determined by normalizing to glyceraldehyde 3-phosphate dehydrogenase mRNA levels. Primer sequences used for qPCR analysis are shown in Supplementary Table 2.

Reverse transcription PCR analysis of S1PRs. Total RNA was isolated from MCF-7 cells using Trizol, according to the manufacturer's instructions. A SuperScript III Fast-Strand Synthesis System (Invitrogen) was used for reverse transcription synthesis of cDNAs. PCR amplification was performed with PrimeStar HS DNA polymerase (Takara) using GeneAmp PCR System 9700 (Applied

Biosystems). The cycling conditions were as follows: 1 min at 95 °C, 40 cycles of 30 s at 95 °C, 30 s at 54–66 °C, 1 min at 72 °C, following 7 min at 72 °C. Primer sequences used for reverse transcription PCR analysis are shown in Supplementary Table 2.

Transient RNA interference. Double-strand RNA oligonucleotides (siRNAs) against *S1PR3*, *S1PR2* and appropriate control scrambled siRNA were from Santa Cruz Biotechnology. The siRNAs against *Notch1*, *ABCC1* and *Spns2* were from Invitrogen. The siRNAs were transfected into MCF-7 cells using RNAiMax (Invitrogen) according to the manufacturer's recommendations.

Stable knockdown by lentiviral shRNA transduction. For stable gene silencing of *S1PR3* or *S1PR2*, specific shRNA MISSION lentiviruses (Sigma-Aldrich) were transduced into cells. The target sequence was 5′-CCGGGATCCTCTACGCAC GCATCTACTCGAGTAGATGCGTGCGTAGAGGATCTTTTTG-3′ for sh*S1PR3* and 5′-CCGGACTTTACCACCTGGTACAAAGCTCGAGCTTTGTACCAGGTG GTAAAGTTTTTTG-3′ for sh*S1PR2*. The transduced cells were selected in growth medium containing 1.5 μg ml^{-1} puromycin (Sigma-Aldrich).

Immunoblot analysis. Cells were lysed in Cell Lysis Buffer (Cell Signaling Technology) on ice for 30 min. Lysates were subjected to sodium dodecyl sulphate polyacrylamide gel electrophoresis and transferred to Immobilon-P Transfer Membrane (Millipore). Membranes were blocked with 5% (w/v) bovine serum albumin in Tris-buffered saline containing 0.1% Tween-20 (TBST) and incubated with primary antibodies overnight at 4 °C. Membranes were then incubated with horseradish peroxidase-conjugated secondary antibodies (Cell Signaling Technology, 1:2,000) for 1 h at room temperature and detected using ECL Prime Western Blotting Detection Reagent (GE Healthcare). Images were acquired using a LAS-3000 Imager (Fujifilm). The density of each band was quantified using an image analyser (Multi Gauge software, Fujifilm). The primary antibodies used were S1PR3 (#sc-30024, 1:2,000), S1PR2 (#sc-25491, 1:1,000), Notch1 (#4380, 1:1,000), N1ICD (#2421, 1:1,000), Notch3 (#2889, 1:1,000), FLAG (#F1804, 1:1,000), myc (#C3956, 1:5,000), HA (#H6908, 1:1,000), phospho-ADAM17 (#SAB4504073, 1:1,000), ADAM17 (#AB19027, 1:1,000), phospho-p38MAPK (#9211, 1:1,000), p38MAPK (#9212, 1:1,000), phospho-Akt (#9271, 1:1,000), Akt (#9272, 1:1,000), SphK1 (#AP7237c, 1:500), SphK2 (a gift from Dr T. Okada at Kobe University, 1:3,000), ABCC1 (#ab3368, 1:1,000), Spns2 (#sc-130102, 1:1,000) and β-actin (#A5441, 1:10,000). Original immunoblots are shown in Supplementary Fig. 19.

Immunocytochemistry. SphK-overexpressing MCF-7 cells and mammosphere cells were plated on glass coverslips. Cells were fixed with 4% paraformaldehyde and permeabilized with 0.2% Triton X-100. Coverslips were blocked with 5% FBS and incubated overnight at 4 °C with primary antibodies that recognized FLAG (#F1804, 1:500), HA (#H6908, 1:120), SphK1 (#ab46719, 1:50), S1PR3 (#sc-30024, 1:50), ALDH1 (#611194, 1:100). ADAM17 (#ab57484, 1:300) and activated Notch1 (#ab8925, 1:200). After rinsing with PBS, coverslips were incubated for 1 h at room temperature with Alexa488-conjugated (#A11034, 1:200) or Alexa555-conjugated (#A21424, 1:200) secondary antibody. In the case of triple staining of Sphk1, ALDH1 and N1ICD, antibody to SphK1 was labelled with AMCA conjugation kit (Abcam). After rinsing with PBS, coverslips were incubated with AMCA-conjugated SphK1 antibody (1:100) for 1.5 h. Nuclei were counterstained with DAPI (Nacalai Tesque). Fluorescence images were obtained using a Nikon A1 confocal microscope (Nikon).

Immunoprecipitation assay. Immunoprecipitation was conducted as previously reported with slight modifications[51]. MCF-7 cells were transfected with myc-tagged ADAM17. At 48 h after transfection, cells were lysed in lysis buffer (20 mM Tris–HCl pH 7.4, 200 mM NaCl, 0.1% NP-40, 10 mM NaF, 1 mM Na_3VO_4 and complete mini protease inhibitor cocktail (Roche Applied Sciences)). Lysates (100 μg) were incubated with myc-specific polyclonal antibody (#C3956, 1 μg) or normal rabbit IgG (#PM035, MBL, 1 μg) overnight at 4 °C. Subsequently, Protein G Sepharose (Amersham Pharmacia Biotech) was added to the mixture and incubated for an additional 2 h at 4 °C. Beads were washed with lysis buffer and immunoprecipitated proteins analysed by immunoblotting using a p38MAPK-specific polyclonal antibody (#9212) and a myc-specific polyclonal antibody (#C3956).

ADAM17 activity. ADAM17 activity was measured using a SensoLyte 520 ADAM17 Activity Assay Kit (ANASPEC) according to the manufacture's instruction[52]. MCF-7 cells were scraped in PBS containing a complete mini protease inhibitor cocktail and lysed using five cycles of freeze–thawing. Lysed cells were centrifuged at 20,000 *g* for 15 min and pelleted membranes resuspended with assay buffer. Approximately 15 μg of proteins were mixed with substrate for 30 min and fluorescence intensity was measured using a Wallac1420ARVO fluoroscan (Perkin Elmer), with excitation at 490 nm and emission at 520 nm.

γ-secretase activity. The activity of γ-secretase was measured using a specific fluorogenic substrate assay[53]. Cells were collected in cell lysis buffer containing (20 mM HEPES pH 7.0, 150 mM KCl, 2 mM EDTA, 1% (3-cholamidopropyl) dimethylammonio]-2-hydroxy-1-propanesulfonate (CHAPSO; Dojindo Laboratories), and complete Mini, EDTA-free protease inhibitor cocktail (Roche)). Lysates were centrifuged at 10,000 *g* for 1 min at 4 °C to remove nuclei and large cell debris. Approximately 5 μg of protein was added to each well of a white 96-well polystyrene microplate (Packard) and an equal volume of assay buffer (50 mM Tris–HCl (pH 6.8), 2 mM EDTA, and 0.25% (3-cholamidopropyl) dimethylammonio]-2-hydroxy-1-propanesulfonate (w/v)) added. 10 μM fluorogenic γ-secretase substrate (Peptide) was added to the plate and samples incubated at 37 °C for 4 h in the dark. Fluorescence intensity was measured using a Wallac1420ARVO fluoroscan (Perkin Elmer) with excitation at 355 nm and emission at 460 nm.

SphK activity. SphK activity was measured using omega-(7-nitro-2-1,3-benzoxadiazol-4-yl)-D-erythro-sphingosine-labelled fluorescent substrate[54]. Cells were lysed with a single freeze–thaw cycle in 50 mM HEPES (pH 7.4), 10 mM KCl, 15 mM $MgCl_2$, 0.1% Triton X-100, 20% glycerol, 2 mM orthovanadate, 2 mM dithiothreitol, 10 mM NaF, 1 mM deoxypyridoxine and complete Mini, EDTA-free protease inhibitor cocktail (Roche). The lysate was cleared by centrifuging at 20,000 *g* for 15 min at 4 °C. SphK1 activity was measured in 50 mM HEPES (pH 7.4), 15 mM $MgCl_2$, 0.5% Triton X-100, 10% glycerol, 5 mM NaF, 1 mM deoxypyridoxine, 2 mM ATP and 10 μM NBD-sphingosine (Avanti Polar Lipids). SphK2 activity was measured in 50 mM HEPES (pH 7.4), 15 mM $MgCl_2$, 0.5 M KCl, 10% glycerol, 5 mM NaF, 1 mM deoxypyridoxine, 2 mM ATP and 10 μM NBD- sphingosine. Reactions were started with the addition of 5 μg of lysate protein and incubated for 4 h at room temperature. Reactions were extracted with the addition of 1 M potassium phosphate (pH 8.5), followed by chloroform/methanol (2:1), then cleared at 15,000 *g* for 1 min. The upper aqueous layer was placed into the wells of white 96-well polystyrene microplates (Packard). Fluorescence intensity was measured with a Wallac1420ARVO fluoroscan (Perkin Elmer) with excitation at 485 nm and emission at 535 nm.

Tumorigenicity assay. The animal study protocol was reviewed and approved by the animal care and use committee of the institute. Six-week-old female Balb/c nude mice (CLEA Japan) were used in these studies and were given injections of 17-β-estradiol (Sigma-Aldrich) dissolved in pure sesame oil (0.1 mg 0.05 ml^{-1} sesame oil per mouse, subcutaneously) 1 day before tumour inoculation, and at weekly intervals, according to a previously reported protocol with slight modifications[55]. The ALDH-positive cell population was sorted by FACS (BD Aria II) and suspended in PBS mixed with an equal volume of Matrigel (BD Biosciences). Mice were given bilateral subcutaneous injections of 1×10^5 (0.1 ml) cells. Tumour growth was monitored for 6 weeks and analysed. Tumour volume was determined using the formula: $V = ½ \times$ larger diameter $\times$ (smaller diameter)^2.

For the immunohistochemistry, paraffin-embedded sections of breast tumours from xenografts were deparaffinized in xylene and rehydrated in graded alcohol. Antigen retrieval was conducted three times by microwaving the slides in 0.01 M citrate buffer (pH 6.0) for 5 min. Sections were blocked with 5% FBS and incubated for 1.5 h with primary antibodies that recognized S1PR3 (#sc-30024, 1:50) and ALDH1 (#611194, 1:100). After rinsing with PBS, coverslips were incubated for 1 h at room temperature with Alexa488-conjugated (#A11034, 1:200) or Alexa555-conjugated (#A21424, 1:200) secondary antibody. Nuclei were counterstained with DAPI (Nacalai Tesque). Fluorescence images were obtained using a Biorevo BZ-9000 (Keyence). The number of S1PR3- and ALDH1 double-positive cells was counted in five fields[56].

For the hierarchy assay, the xenografts were collected after 6 weeks, dissociated into single cells and TRA-1-85-positive cells analysed using the ALDH assays[57]. Single cells were suspended in ALDH assay buffer containing the BAAA (1 μM) and incubated 30 min at 37 °C. The cells were resuspended in ALDH assay buffer for subsequent staining with the APC-conjugated TRA-1-85 antibody (#FAB3195A, 1:10), which recognizes human cells and thereby allows their discrimination from mouse cells. After incubation for 30 min and following centrifugation, the cells were resuspended in ALDH assay buffer containing 7-AAD (BD Bioscience, #559925) and analysed with a FACS Aria II cell sorter (BD Bioscience).

For the chronic administration, TY52156 (167 mg ml^{-1} in a 1:1 mixture of DMSO and PEG400) was inserted in subcutaneously implanted Alzet osmotic pumps (Cupertino), designed to release TY52156 continuously (at about 25 μg h^{-1}) for 6 weeks.

Mammosphere formation from primary cells. Mammosphere formation using primary cells (Celprogen) was performed[7,8]. The cells were plated as single cells in ultralow attachment dishes (Corning) at a density of 20,000 viable cells ml^{-1} in mammary epithelial growth medium for 7 days. To make secondary mammospheres, primary mammospheres were collected by gentle centrifugation (200*g*), dissociated enzymatically (10 min in 0.05% trypsin–EDTA) and mechanically (pipetting with yellow tips) into a single-cell suspension. The cells obtained from dissociation were then seeded in ultralow attachment dishes in mammary epithelial growth medium again.

Statistical analysis. Results are shown as mean ± s.d. For tumour incidence, the *P* value was calculated using the Fisher's exact test (Fig. 6a,g,h). Bonferroni correction was applied for multiple comparisons (Fig. 6a,g). For tumour volume, the *P* value was calculated using the Kruskal–Wallis test, followed by *post hoc* Steel–Dwass's multiple comparison test (Fig. 6c). Differences at $P<0.05$ were considered to be significant. Statistical analyses were performed using Excel 2010 with the add-in software.

References

1. Visvader, J. E. & Lindeman, G. J. Cancer stem cells in solid tumours: accumulating evidence and unresolved questions. *Nat. Rev. Cancer* **8,** 755–768 (2008).
2. Bonnet, D. & Dick, J. E. Human acute myeloid leukemia is organized as a hierarchy that originates from a primitive hematopoietic cell. *Nat. Med.* **3,** 730–737 (1997).
3. Al-Hajj, M. *et al.* Prospective identification of tumorigenic breast cancer cells. *Proc. Natl Acad. Sci. USA* **100,** 3983–3988 (2003).
4. Ginestier, C. *et al.* ALDH1 is a marker of normal and malignant human mammary stem cells and a predictor of poor clinical outcome. *Cell Stem Cell* **1,** 555–567 (2007).
5. Jiang, F. *et al.* Aldehyde dehydrogenase 1 is a tumour stem cell-associated marker in lung cancer. *Mol. Cancer Res.* **7,** 330–338 (2009).
6. van den Hogen, C. *et al.* High aldehyde dehydrogenase activity identifies tumour-initiating and metastasis-initiating cells in human prostate cancer. *Cancer Res.* **70,** 5163–5173 (2010).
7. Hinohara, K. *et al.* ErbB receptor tyrosine kinase/NF-κB signaling controls mammosphere formation in human breast cancer. *Proc. Natl Acad. Sci. USA* **109,** 6584–6589 (2012).
8. Dontu, G. *et al. In vitro* propagation and transcriptional profiling of human mammary stem/progenitor cells. *Genes Dev.* **17,** 1253–1270 (2003).
9. Takebe, N. & Ivy, S. P. Controversies in cancer stem cells: targeting embryonic signaling pathways. *Clin. Cancer Res.* **16,** 3106–3112 (2010).
10. Scheel, C. *et al.* Paracrine and autocrine signals induce and maintain mesenchymal and stem cell states in the breast. *Cell* **145,** 926–940 (2011).
11. Takabe, K., Paugh, S. W., Milstian, S. & Spiegel, S. 'Inside-out' signalling of sphingosine-1-phosphate: therapeutic targets. *Pharmacol. Rev.* **60,** 181–195 (2008).
12. Kohama, T. *et al.* Molecular cloning and functional characterization of murine sphingosine kinase. *J. Biol. Chem.* **273,** 23722–23728 (1998).
13. Liu, H. *et al.* Molecular cloning and functional characterization of a novel mammalian sphingosine kinase type 2 isoform. *J. Biol. Chem.* **275,** 19513–19520 (2000).
14. Pyne, N. J. & Pyne, S. Sphingosine 1 phosphate and cancer. *Nat. Rev. Cancer* **10,** 489–503 (2010).
15. Fyrst, H. & Saba, J. D. An update on sphingosine-1-phosphate and other sphingolipid mediators. *Nat. Chem. Biol.* **6,** 489–497 (2010).
16. Nagahashi, M. *et al.* Sphingosine-1-phosphate produced by sphingosine kinase 1 promotes breast cancer progression by stimulating angiogenesis and lymphangiogenesis. *Cancer Res.* **72,** 726–735 (2012).
17. Charafe-Jauffret, E. *et al.* Breast cancer cell lines contain functional cancer stem cells with metastatic capacity and a distinct molecular signature. *Cancer Res.* **69,** 1302–1313 (2009).
18. Hirata, N., Sekino, Y. & Kanda, Y. Nicotine increases cancer stem cell population in MCF-7 cells. *Biochem. Biophys. Res. Commun.* **403,** 138–143 (2010).
19. Long, J. S. *et al.* Sphingosine 1-phosphate receptor 4 uses HER2 (ERBB2) to regulate extracellular signal regulated kinase-1/2 in MDA-MB-453 breast cancer cells. *J. Biol. Chem.* **285,** 35957–35966 (2010).
20. Lin, C. I., Chen, C. N., Lin, P. W. & Lee, H. Sphingosine-1-phosphate regulates inflammation-related genes in human endothelial cells thorough S1P1 and S1P3. *Biochem. Biophys. Res. Commun.* **355,** 895–901 (2007).
21. Murakami, A. *et al.* Sphingosine 1-phosphate (S1P) regulates vascular contraction via S1P3 receptor: investigation based on a new S1P3 receptor antagonist. *Mol. Pharmacol.* **77,** 704–713 (2010).
22. Pannuti, A. *et al.* Targeting Notch to target cancer stem cells. *Clin. Cancer Res.* **16,** 3141–3152 (2010).
23. Noseda, M. *et al.* Smooth muscle α-actin is a direct target of Notch/CSL. *Circ. Res.* **98,** 1468–1470 (2006).
24. Jefflies, S., Robins, D. J. & Capobianco, A. J. Characterization of a high-molecular-weight Notch complex in the nucleus of Notch^{ic}-transformed RKE cells and in a human T-cell leukemia cell line. *Mol. Cell. Biol.* **22,** 3927–3941 (2002).
25. Artavanis-Tsakonas, S. & Muskavitch, M. A. Notch: the past, the present, and the future. *Curr. Top. Dev. Biol.* **92,** 1–29 (2010).
26. Ladi, E. *et al.* The divergent DSL ligand Dll3 does not activate Notch signaling but cell autonomously attenuates signaling induced by other DSL ligands. *J. Cell Biol.* **170,** 983–992 (2005).
27. Liu, C. *et al.* TACE-mediated ectodomain shedding of the type I TGF-β receptor downregulates TGF-β signaling. *Mol. Cell* **35,** 25–36 (2009).
28. Lammich, S. *et al.* Constitutive and regulated α-secretase cleavage of Alzheimer's amyloid precursor protein by a disintegrin metalloprotease. *Proc. Natl Acad. Sci. USA* **96,** 3922–3927 (1999).
29. Diaz-Rodriguez, E. *et al.* Extracellular signal-regulated kinase phosphorylates tumour necrosis factor alpha-converting enzyme at threonine 735: a potential role in regulated shedding. *Mol. Biol. Cell* **13,** 2031–2044 (2002).
30. Fan, H., Turck, C. W. & Derynck, R. Characterization of growth factor-induced serine phosphorylation of tumour necrosis factor-alpha converting enzyme and of an alternatively translated polypeptide. *J. Biol. Chem.* **278,** 18617–18627 (2003).
31. Xu, P. & Derynck, R. Direct activation of TACE-mediated ectodomain shedding by p38 MAP kinase regulates EGF receptor-dependent cell proliferation. *Mol. Cell* **37,** 551–566 (2010).
32. Pitson, S. M. *et al.* Phosphorylation-dependent translocation of sphingosine kinase to the plasma membrane drives its oncogenic signaling. *J. Exp. Med.* **201,** 49–54 (2005).
33. Igarashi, N. *et al.* Sphingosine kinase 2 is a nuclear protein and inhibits DNA synthesis. *J. Biol. Chem.* **278,** 46832–46839 (2003).
34. Takabe, K. *et al.* Estradiol induces export of sphingosine 1-phosphate from breast cancer cells via ABCC1 and ABCG2. *J. Biol. Chem.* **285,** 10477–10486 (2010).
35. Kawahara, A. *et al.* The sphingolipid transporter spns2 functions in migration of zebrafish myocardial precursors. *Science* **323,** 524–527 (2009).
36. Pébay, A. *et al.* Essential roles of sphingosine-1-phosphate and platelet-derived growth factor in the maintenance of human embryonic stem cells. *Stem Cells* **23,** 1541–1548 (2005).
37. Pitson, S. M. & Pébay, A. Regulation of stem cell pluripotency and neural differentiation by lysophospholipids. *Neurosignals* **17,** 242–254 (2009).
38. Bozkulak, E. C. & Weinmaster, G. Selective use of ADAM10 and ADAM17 in activation of Notch1 signaling. *Mol. Cell. Biol.* **29,** 5679–5695 (2009).
39. van Tetering, G. *et al.* Metalloprotease ADAM10 is required for Notch1 site 2 cleavage. *J. Biol. Chem.* **284,** 31018–31027 (2009).
40. Lu, J. *et al.* Endothelial cells promote the colorectal cancer stem cell phenotype through a soluble form of Jagged-1. *Cancer Cell* **23,** 171–185 (2013).
41. Inoue, A. *et al.* TGFα shedding assay: an accurate and versatile method for detecting GPCR activation. *Nat. Methods* **9,** 1021–1029 (2012).
42. Harrison, H. *et al.* Regulation of breast cancer stem cell activity by signaling through the Notch 4 receptor. *Cancer Res.* **70,** 709–718 (2010).
43. Ruckhäberle, E. *et al.* Microarray analysis of altered sphingolipid metabolism reveals prognostic significance of sphingosine kinase 1 in breast cancer. *Breast Cancer Res. Treat.* **112,** 41–52 (2008).
44. Watson, C. *et al.* High expression of sphingosine 1-phosphate receptors, S1P1 and S1P3, sphingosine kinase 1, and extracellular signal-regulated kinase-1/2 is associated with development of tamoxifen resistance in estrogen receptor-positive breast cancer patients. *Am. J. Pathol.* **177,** 2205–2215 (2010).
45. Long, J. S. *et al.* Sphingosine kinase 1 induces tolerance to human epidermal growth factor receptor 2 and prevents formation of a migratory phenotype in response to sphingosine 1-phosphate in estrogen receptor-positive breast cancer cells. *Mol. Cell. Biol.* **30,** 3827–3841 (2010).
46. Goetzl, E. J. *et al.* Dual mechanisms for lysophospholipid induction of proliferation of human breast carcinoma cells. *Cancer Res.* **59,** 4732–4737 (1999).
47. Ranganathan, P., Weaver, K. L. & Capobianco, A. J. Notch signaling in solid tumours: a little bit of everything but not all the time. *Nat. Rev. Cancer* **11,** 338–351 (2011).
48. Debeb, B. G. *et al.* Pre-clinical studies of Notch signaling inhibitor RO4929097 in inflammatory breast cancer cells. *Breast Cancer Res. Treat.* **134,** 495–510 (2012).
49. Ramakrishnan, V. *et al.* MRK003, a γ-secretase inhibitor exhibits promising *in vitro* pre-clinical activity in multiple myeloma and non-Hodgkin's lymphoma. *Leukemia* **26,** 340–348 (2012).
50. Olsauskas-Kuprys, R., Zlobin, A. & Osipo, C. Gamma secretase inhibitors of Notch signaling. *OncoTargets Ther.* **6,** 943–955 (2013).
51. Kanda, Y., Mizuno, K., Kuroki, Y. & Watanabe, Y. Thrombin-induced p38 mitogen-activated protein kinase activation is mediated by epidermal growth factor receptor transactivation pathway. *Br. J. Pharmacol.* **132,** 1657–1664 (2001).
52. Rao, S., Liu, X., Freedman, B. D. & Behrens, E. M. Spleen tyrosine kinase (Syk)-dependent calcium signals mediate efficient CpG-induced exocytosis of tumour necrosis factor α (TNFα) in innate immune cells. *J. Biol. Chem.* **288,** 12448–12458 (2013).
53. Farmery, M. R. *et al.* Partial purification and characterization of gamma-secretase from post-mortem human brain. *J. Biol. Chem.* **278,** 24277–24284 (2003).

54. Don, A. S. *et al.* Essential requirement for sphingosine kinase 2 in a sphongolipid apoptosis pathway activated by FTY720 analogues. *J. Biol. Chem.* **282,** 15833–15842 (2007).
55. Zhou, J. *et al.* Activation of the PTEN/mTOR/STAT3 pathway in breast cancer stem-like cells is required for viability and maintenance. *Proc. Natl Acad. Sci. USA* **104,** 16158–16163 (2007).
56. Ahn, G. & Brown, J. M. Matrix metalloproteinase-9 is required for tumour vasculogenesis but not for angiogenesis: role of bone marrow-derived myelomonocytic cells. *Cancer Cell* **13,** 193–205 (2008).
57. Prasmickaite, L. *et al.* Aldehyde dehydrogenase (ALDH) activity does not select for cells with enhanced aggressive properties in malignant melanoma. *PLoS ONE* **5,** e10731 (2010).

Acknowledgements

We thank Dr Taro Okada for his helpful comments on the manuscript. We thank Stuart M. Pitson (University of Adelaide), Taro Okada (Kobe University), Aly Karsan (British Columbia Cancer Research Centre), Anthony J. Capobianco (University of Pennsylvania), Spyros Artavanis-Tsakonas (Harvard Medical School), Stefan Lichtenthaler (Ludvig Maximilians University), Lothar J. Strobl (German Research Center for Environmental Health), Michael J. Hendzel (University of Alberta), Rik Derynck (University of California, San Francisco), and J. Silvio Gutkind (National Institutes of Health) for providing the plasmids. We thank Dr Junya Kanda (Jichi Medical University) for assistance with statistical analyses. We also thank additional members of the laboratory and other members of the Institute for their advice and discussion. This work was supported by the Advanced research for medical products Mining Programme of the National Institute of Biomedical Innovation (NIBIO, #09-02 to Y.K.), a Grant-in-Aid for Scientific Research from the Ministry of Education, Culture, Sports, Science, and Technology, Japan (#23590322, #26670041 to Y.K.), a Health and Labour Sciences Research Grant from the Ministry of Health, Labour and Welfare, Japan (Y.K.), and a grant from the Smoking Research Foundation (Y.K.).

Author contributions

N.H. performed most of the experiments. Y.K. planned the project. Y.K. and Y.S. wrote the manuscript. S.Y. performed the experiments related to ADAM17 mutants. T.S. and M.K. performed the experiments related to TY52156. All authors participated in the preparation of the manuscript.

Additional information

Accession codes: Microarray data have been deposited in the NCBI Gene Expression Omnibus database under accession codes GSE59653.

Supplementary Information accompanies this paper at http://www.nature.com/naturecommunications

Competing financial interests: The authors declare no competing financial interests.

Reprints and permission information is available online at http://npg.nature.com/reprintsandpermissions/

How to cite this article: Hirata, N. *et al.* Sphingosine-1 phosphate promotes expansion of cancer stem cells via S1PR3 by a ligand-independent Notch activation. *Nat. Commun.* 5:4806 doi: 10.1038/ncomms5806 (2014).

Journal of Molecular and Cellular Cardiology 77 (2014) 178–191

Contents lists available at ScienceDirect

Journal of Molecular and Cellular Cardiology

journal homepage: www.elsevier.com/locate/yjmcc

Original article

Image-based evaluation of contraction–relaxation kinetics of human-induced pluripotent stem cell-derived cardiomyocytes: Correlation and complementarity with extracellular electrophysiology

Tomohiro Hayakawa [a,*,1], Takeshi Kunihiro [a,1], Tomoko Ando [b], Seiji Kobayashi [a], Eriko Matsui [a], Hiroaki Yada [a], Yasunari Kanda [b], Junko Kurokawa [b], Tetsushi Furukawa [b,**]

[a] Medical Business Unit, Sony Corporation, 1-5-45 Yushima, Bunkyo-ku, Tokyo 113-8510, Japan
[b] Department of Bio-informational Pharmacology, Medical Research Institute, Tokyo Medical and Dental University, 1-5-45 Yushima, Bunkyo-ku, Tokyo 113-8510, Japan

ARTICLE INFO

Article history:
Received 27 July 2014
Accepted 10 September 2014
Available online 23 September 2014

Keywords:
Human-induced pluripotent stem cell-derived cardiomyocytes
Motion vector prediction
Traction force microscopy
Ca^{2+} transient
Field potential
Multi-electrode arrays

ABSTRACT

In this study, we used high-speed video microscopy with motion vector analysis to investigate the contractile characteristics of hiPS-CM monolayer, in addition to further characterizing the motion with extracellular field potential (FP), traction force and the Ca^{2+} transient. Results of our traction force microscopy demonstrated that the force development of hiPS-CMs correlated well with the cellular deformation detected by the video microscopy with motion vector analysis. In the presence of verapamil and isoproterenol, contractile motion of hiPS-CMs showed alteration in accordance with the changes in fluorescence peak of the Ca^{2+} transient, i.e., upstroke, decay, amplitude and full-width at half-maximum. Simultaneously recorded hiPS-CM motion and FP showed that there was a linear correlation between changes in the motion and field potential duration in response to verapamil (30–150 nM), isoproterenol (0.1–10 μM) and E-4031 (10–50 nM). In addition, tetrodotoxin (3–30 μM)-induced delay of sodium current was corresponded with the delay of the contraction onset of hiPS-CMs. These results indicate that the electrophysiological and functional behaviors of hiPS-CMs are quantitatively reflected in the contractile motion detected by this image-based technique. In the presence of 100 nM E-4031, the occurrence of early after-depolarization-like negative deflection in FP was also detected in the hiPS-CM motion as a characteristic two-step relaxation pattern. These findings offer insights into the interpretation of the motion kinetics of the hiPS-CMs, and are relevant for understanding electrical and mechanical relationship in hiPS-CMs.

1. Introduction

Human-induced pluripotent stem cell-derived cardiomyocytes (hiPS-CMs) and human embryonic stem cell-derived cardiomyocyte (hES-CMs) hold promise for the applications in cardiac cell biology [1], drug development [2–6] and cardiac therapeutics [7–11]. To date, hiPS-/hES-CMs have been characterized largely based on studies that examined the aspects of the electrophysiology or the Ca^{2+} signaling/handling [3,12–20]. This is in contrast to the contractile characteristics of the hiPS-/hES-CMs, as there have been few studies performed at the present time [21–29]. Limited numbers of studies, however, demonstrated that hES-CMs showed chronotropy but no significant inotropy in response to β-adrenoceptor agonist, isoproterenol, by using a force transducer for three-dimensionally (3D) engineered hES-CM tissue [29] or for co-culture system of hES-CMs with non-contractile slices of neonatal murine ventricles [28]. These results suggest the importance of performing a phenotype evaluation for hiPS-/hES-CMs based on the contractile properties as well as electrophysiological characteristics to assess their adaptability to the applications. In addition, a report that used atomic force microscopy to investigate two-dimensionally (2D) cultured hiPS-CMs from patients with dilated cardiomyopathy (DCM) demonstrated that the DCM hiPS-CM exhibited a phenotype that was based on the perturbed contractility rather than on the electrophysiological abnormality [27,30]. This demonstrated the need for developing methodologies that characterize the electrical and mechanical relationship of hiPS-/hES-CMs.

In our current study, we combined phase-contrast video microscopy and multi-electrode array (MEA) measurement in order to investigate the relationship between the contractile motion and the extracellular

Abbreviations: ADD, average deformation distance; CM, cardiomyocyte; CRD, contraction–relaxation duration; FP, field potential; FPD, field potential duration; FP_{slow}, slow signal component of FP; FWHM, full-width at half-maximum; hiPS-CM, human-induced pluripotent stem cell-derived cardiomyocyte; hES-CM, human embryonic stem cell-derived cardiomyocyte; MCS, maximum contraction speed; MEA, multi-electrode array; MRS, maximum relaxation speed; PIV, particle image velocimetry; TF, traction force; TFM, traction force microscopy; TTX, tetrodotoxin.

* Corresponding author. Tel.: +81 3 5803 4791; fax: +81 3 5803 4790.
** Corresponding author. Tel.: +81 3 5803 4950; fax: +81 3 5803 0364.
E-mail addresses: tomohiro.hayakawa@jp.sony.com (T. Hayakawa), t_furukawa.bip@mri.tmd.ac.jp (T. Furukawa).
[1] These authors contributed equally.

http://dx.doi.org/10.1016/j.yjmcc.2014.09.010

electrophysiology of the 2D-cultured hiPS-CMs under various cardioactive agents. The label-free video microscopy is a method of choice for evaluating the contractile characteristics of CMs, and many researchers have reported the applicability in various culture conditions [31–40]. For example, for isolated rod-shaped adult CMs, the shortening length and velocity of contraction of whole cell body or sarcomere were evaluated quantitatively using video microscopy with edge-detection technique [34,41–43]. Edge-detection method was also applied to the contractility estimation of embryonic bodies with hES-CMs [44,45]. Kamgoue et al. applied image correlation analysis for single adult and neonatal rat CMs, and detected intracellular strains quantitatively from the calculated 2D displacement field [36]. Modified image correlation analysis was developed by Ahola et al. for single hiPS-CMs, which exhibits heterogeneous in shape, to evaluate the detailed intracellular deformation [46]. Beating frequency of mouse ES-CM monolayer has been evaluated based on the image analysis of transmitted light intensity change [35] and the fast Fourier transform technique [39]. Meanwhile, we have previously reported the applicability of image correlation analysis, or motion vector analysis, for analyzing video images of neonatal rat CM monolayers [47]. By calculating the velocity field over the whole image, this method has made it possible to evaluate the average contractile speed, global deformation and contraction propagation in the CM monolayer with high spatiotemporal resolution [47]. Due to the convenience and non-invasiveness, such label-free video microscopies would be advantageous for the readout method of hiPS-/hES-CM behaviors, especially for the applications in therapeutics and drug safety assessment. In addition, since microscope observation itself does not interfere with the electrophysiological measurements, video microscopies are amenable to the simultaneous measurement with electrical measurements, e.g., patch clamping and MEA, to gain greater insight into the electro-mechanical correlations of CMs.

In this study, we further performed traction force microscopy and Ca^{2+} imaging in the hiPS-CMs in order to discuss the association of contractile motion to force development and Ca^{2+} transient, respectively. Our results showed that electrophysiological and functional behaviors of the 2D-cultured hiPS-CMs are quantitatively reflected by contractile motions detected with high-speed video microscopy. These findings offer insights into the interpretation of motion kinetics of hiPS-CMs, and are relevant for understanding electrical and mechanical relationship in hiPS-CMs. These results also demonstrate that it is possible for us to broaden the scope of application for hiPS-CMs for use in even simple culture conditions.

2. Materials and methods

2.1. hiPS-CMs and cell preparation

The hiPS-CMs used in this study were purchased from Cellular Dynamics International, Inc. (CDI) (iCell Cardiomyocytes, CDI, Madison, WI, USA). The iCell CMs are highly purified human CMs (>98% pure cardiomyocytes) that are derived from iPS cells using previously described differentiation and purification protocols [48]. The iCell CMs were seeded and maintained according to the protocol recommended by the supplier using iCell Cardiomyocytes Plating Medium (CDI) and iCell Cardiomyocytes Maintenance Medium (CDI) at 37 °C, 7% CO_2. The details on the cell preparation for MEA recordings, Ca^{2+} transient measurements and TFM are provided in the Supplementary materials.

2.2. Video microscopy

A high-speed digital CMOS camera (KP-FM400WCL, Hitachi Kokusai Denki Engineering, Tokyo, Japan) was mounted on an inverted microscope (Eclipse Ti, Nikon, Tokyo, Japan). Movie images of beating hiPS-CMs were recorded as sequential phase-contrast images with a 10× objective at a frame rate of 150 fps, a resolution of 2048 × 2048 pixels, and a depth of 8 bits. Further details on the video imaging are provided in the Supplementary materials.

2.3. Motion vector analysis

Motion vectors of beating hiPS-CMs were obtained using a block matching algorithm, as has been described elsewhere [47,49]. Further details on the motion vector analysis are provided in the Supplementary materials.

2.4. Traction force microscopy

2.4.1. Fabrication of polyacrylamide hydrogel substrates and hiPS-CM seeding

Polyacrylamide hydrogel substrates containing fluorescence beads (#G0100, 1 μm diameter, Ex/Em = 468/508 nm, Duke Scientific Co., CA, USA) were fabricated in accordance with previously reported methods [26,50,51]. Further details on the methods are provided in the Supplementary materials.

2.4.2. Traction force microscopy

Video of the hiPS-CMs cultured on polyacrylamide gel was captured using phase-contrast and fluorescence microscopy to detect contractile motion and substrate deformation, respectively. Estimation of the force development of hiPS-CMs was performed by a particle image velocimetry (PIV) [52] and Fourier transform traction cytometry (FTTC) [51–53] programs implemented as an ImageJ plugin. Details are provided in the Supplementary materials.

2.5. Simultaneous recordings of FP and motion

MED probes (MED-P515A, Alpha MED Sciences, Osaka, Japan) equipped with platinum black-coated 64 planar microelectrodes that were arranged in an 8 × 8 grid embedded in the center of a transparent glass plate were used for extracellular recordings of the FP from the CM monolayer [54]. The details on the cell preparation for MEA recordings are provided in the Supplementary materials. Image acquisitions and multi-electrode array (MEA) recordings were synchronized using external triggering options of the MEA system. Data were recorded simultaneously for the 64 electrodes (sampling frequency; 20 kHz, bandwidth; 1–1000 Hz) and were analyzed by Mobius Software (Alpha MED Sciences) in order to detect the field potential duration (FPD). In this study, we averaged at least 10 consecutive FP waveforms to evaluate the field potential parameters. The details on the simultaneous measurements are also provided in the Supplementary materials.

2.6. Calcium imaging

For imaging of the Ca^{2+} transient in the hiPS-CMs, iCell Cardiomyocytes (CDI) were plated in a 96-well plate pre-coated with rat collagen type I (BD, Franklin lakes, NJ) at a density of 3×10^4 cells/well (cultured with 100 μl medium). hiPS-CMs were loaded with Fluo-5F/AM (Invitrogen, Carlsbad, CA, USA) dissolved in dimethylsulfoxide (DMSO, WAKO Pure Chemical, Osaka, Japan) and added to the culture medium at a concentration of 5 μM in preparation for the Ca^{2+} imaging. After 30 min incubation, the culture dishes were placed on a microscope stage (IX-71, Olympus, Tokyo, Japan). Ca^{2+} fluorescence images were captured with a digital CCD camera (CoolSNAP HQ2, Photometrics, Tucson, AZ, USA) at a resolution of 696 × 520 pixels and 33 fps using a 20× objective and recorded using MetaMorph software (Molecular Devices, Sunnyvale, CA, USA). The data were then quantified as the background subtracted fluorescence intensity changes (ΔF) normalized to the baseline fluorescence (F_0) using the ImageJ software and the KaleidaGraph software ver. 4.1.1 (Synergy Software, Reading, PA, USA). Amplitudes, full-width at half-

maximum, maximal upstroke and the decay of the Ca^{2+} transient were also analyzed with the KaleidaGraph software.

2.7. Cardioactive substances

Isoproterenol was purchased from Sigma (St. Louis, MO, USA), E-4031 and tetrodotoxin from WAKO Pure Chemical Industries, and verapamil from Nacalai Tesque (Kyoto, Japan). Stock solutions for isoproterenol and E-4031 were prepared in distilled water, while verapamil was prepared in DMSO. All stock solutions were further diluted in culture medium, with the final concentration of DMSO less than 0.05%. Four to six increasing concentrations of the test substances were applied consecutively for 10 min each.

2.8. Statistical analysis

Data are compared to control in the paired *t*-test for the grouped data. Data are presented as means ± SEM. The value was expressed as a percentage of the control value, while the comparison was made using raw values of each parameter. We considered *p* values less than 0.05 to be statistically significant.

3. Results

3.1. Motion vector detection as a reliable representation of contractile characteristics of hiPS-CMs

3.1.1. Motion vector detection from the movie image of single hiPS-CMs

We first evaluated the contractile motion of single hiPS-CMs. Sparsely plated hiPS-CMs exhibited heterogeneous shapes and a variety of sizes (Fig. 1A). Fig. 1B shows an example of single hiPS-CM motion detected by the motion vector analysis. As indicated by the motion vectors that overlay the image of hiPS-CM, cellular deformation generally occurred toward the center direction of the cell body during contraction process (Fig. 1B (1)). After a transient pause of cellular motion (Fig. 1B (2)), the cell body returned to the position of resting state, exhibiting a slower motion speed than that observed during contraction (Fig. 1A (3)). By averaging the magnitude of motion vectors and plotting them against time, we were able to obtain information on the contraction and relaxation motion (Fig. 1C), along with the frequency (Fig. 1D). Although the contraction and relaxation occurs in the opposite direction, the average of vector magnitude is a positive value, thereby resulting in a two-positive peak profile that reflects the contraction–relaxation process. As seen in Fig. 1E, we are able to extract various parameters regarding contractile motion from this two-peak motion profile. Our current study primarily examined four parameters of this hiPS-CM motion. These included the maximum values of the average magnitude of motion vectors during the contraction (a) and relaxation (b) processes (termed MCS; maximum contraction speed and MRS; maximum relaxation speed, respectively), the total area under two peaks (c) (representing the average deformation distance (ADD) during the contraction–relaxation process), and the duration of contraction and relaxation motion (d) (with the duration between the onset of the contraction peak and the offset of the relaxation peak defined as the contraction–relaxation duration (CRD)). Fig. 1F–I shows contractile parameters of single hiPS-CMs ($n = 40$) cultured in physiological condition (37 °C and 5% CO_2). Single hiPS-CMs exhibited beating rate ranging from ~20 to ~110 beats per minute (bpm) with the average of 62 bpm. Analysis of motion vectors showed that the average values of MCS, MRS, CRD and ADD were 8.2 μm/s, 4.1 μm/s, 455 ms and 1.07 μm, respectively, and the average cell area was found to be 4244.3 μm^2. We examined to plot the cell area against MCS and MRS, and found that contractile speeds were not significantly dependent on the cell area (Fig. 1K). CRD of single hiPS-CMs showed a linear correlation with the beating rate with the correlation coefficient of 0.768 (Fig. 1L).

3.1.2. Contractile motion and traction force of the hiPS-CMs

Subsequently, we used traction force microscopy (TFM) to assess whether the cellular deformation, detected by phase-contrast microscopy and motion vector analysis, was correlated with the force development of hiPS-CMs on the elastic substrate (polyacrylamide gel). Fig. 2 shows a typical image of a hiPS-CM on the gel substrate (12 kPa) examined by phase-contrast (a) and fluorescence microscopy (b). Typical images of displacement and traction force fields that were calculated from the two fluorescence images (taken before and after contraction) are also shown in Fig. 2A(c) and (d), respectively. We then compared the ADD and the traction force of hiPS-CMs on the elastic substrate (12 kPa and 50 kPa). As shown in Fig. 2B, a linear correlation was observed for the traction force and the ADD of the single hiPS-CMs cultured on gel substrates, with a correlation coefficient of 0.737 ($n = 13$) and 0.595 ($n = 12$) for the hiPS-CMs on the 12 kPa and 50 kPa substrates, respectively. These results suggested that the cellular deformation detected with motion vector analysis could be used as a surrogate of the traction force developed by the hiPS-CM contraction.

3.1.3. Ca^{2+} transient and contractile motion of hiPS-CMs

To verify the relationship between the contractile motion and the cytoplasmic Ca^{2+} concentration, we further examined the parameters of the Ca^{2+} transient of the hiPS-CMs. Fig. 3A and B show the typical examples of Ca^{2+} transient and motion waveform of hiPS-CMs, respectively, in the absence and the presence of 100 nM isoproterenol. Isoproterenol altered the amplitude, maximum upstroke, maximum decay and full-width at half-maximum (FWHM) of the Ca^{2+} transient with 113, 114, 157 and 84% of the control, respectively (see bar charts in Fig. 3A). Isoproterenol also altered the contractile parameters, i.e., ADD, MCS, MRS and CRD were changed to 113, 124, 146 and 80% of the control, respectively (Fig. 3B). In contrast, verapamil (100 nM) decreased all of the parameters of Ca^{2+} transient and contractile motion except the decay of Ca^{2+} transient (Fig. 3C and D). As shown in the bar charts in Fig. 3C and D, verapamil altered the Ca^{2+} transient amplitude, upstroke, decay and FWHM with 63, 78, 97 and 66%, respectively, while ADD, MCS, MRS and CRD with 52, 62, 63 and 66%, respectively. These results suggested that the contractile parameters of hiPS-CMs correspond to the intracellular Ca^{2+} status.

3.2. Correlation between the FP and the contractile motion of hiPS-CMs

We next performed a simultaneous recording of the contractile motion and FP using a hiPS-CM monolayer cultured in a MEA dish. To accurately evaluate the relationship between the motion and the FP of hiPS-CMs, the motion vectors were calculated from the hiPS-CMs that were located close to the vicinity of the electrode used for FP data collection. The yellow-squared area (150 × 150 μm) in Fig. 4A represents an example of the region that was used for evaluating contractile motion. Fig. 4B is an enlarged image, in which the calculated motion vectors (fine white bars) are overlaid on the image of the yellow-squared region shown in Fig. 4A. The MCS was ~10 to ~20 μm/s in normal culture conditions (e.g., 37 °C, 5% CO_2 and ~100% humidity) in the absence of any drugs. The simultaneously measured FP exhibited a typical waveform that had a sharp initial negative deflection, which is supposedly correlated with the inward Na^+ current. This is followed by a broad negative deflection (FP_{slow}) and a terminal positive deflection, which is supposedly correlated with the inward Ca^{2+} and outward K^+ currents, respectively [55–58]. As seen in the waveforms presented in Fig. 4C, D and E, several features of the relationship between the motion and the FP of hiPS-CMs were identifiable. These included 1) the CRD was longer than the FPD. The end of the FPD was previously defined as either the peak of the positive deflection [6,54,55,59] or the point where the positive deflection returns to the baseline [60]. The former end-point appears to be correlated with the upstroke of relaxation motion, while the latter end-point appears to be correlated with the peak of relaxation

motion. However, determination of an accurate end-point of FP proved difficult to establish. Other observed features included 2) the onset of the contraction motion follows the occurrence of the Na^+ current peak of the FP (see Fig. 4E), and 3) the position of FP_{slow} occurs with the contraction. The relationships between the motion profiles and the FP for the hiPS-CM described in 1) and 2) were also found in neonatal rat CMs (Supplementary Fig. 2). However, the point 3) was not observed in rats. In the neonatal rat CMs, the entire FP_{slow} was localized within the contraction motion and the broad positive deflection of the FP positions near the end of contraction motion (Supplementary Fig. 2B).

3.3. Correlation between the FP and the contractile motion of hiPS-CMs in the presence of drugs

To determine the correspondence between the contractile motion of the hiPS-CMs and the electrophysiological behavior obtained by the MEA technique, we examined various drugs that are known to inhibit Na^+, K^+ and Ca^{2+} channels.

3.3.1. The effects of a Na^+ channel blocker, tetrodotoxin (TTX)

It has been reported that Na^+ channel blockers decreased the amplitude and slope of the initial negative spike of FP waveform of CM

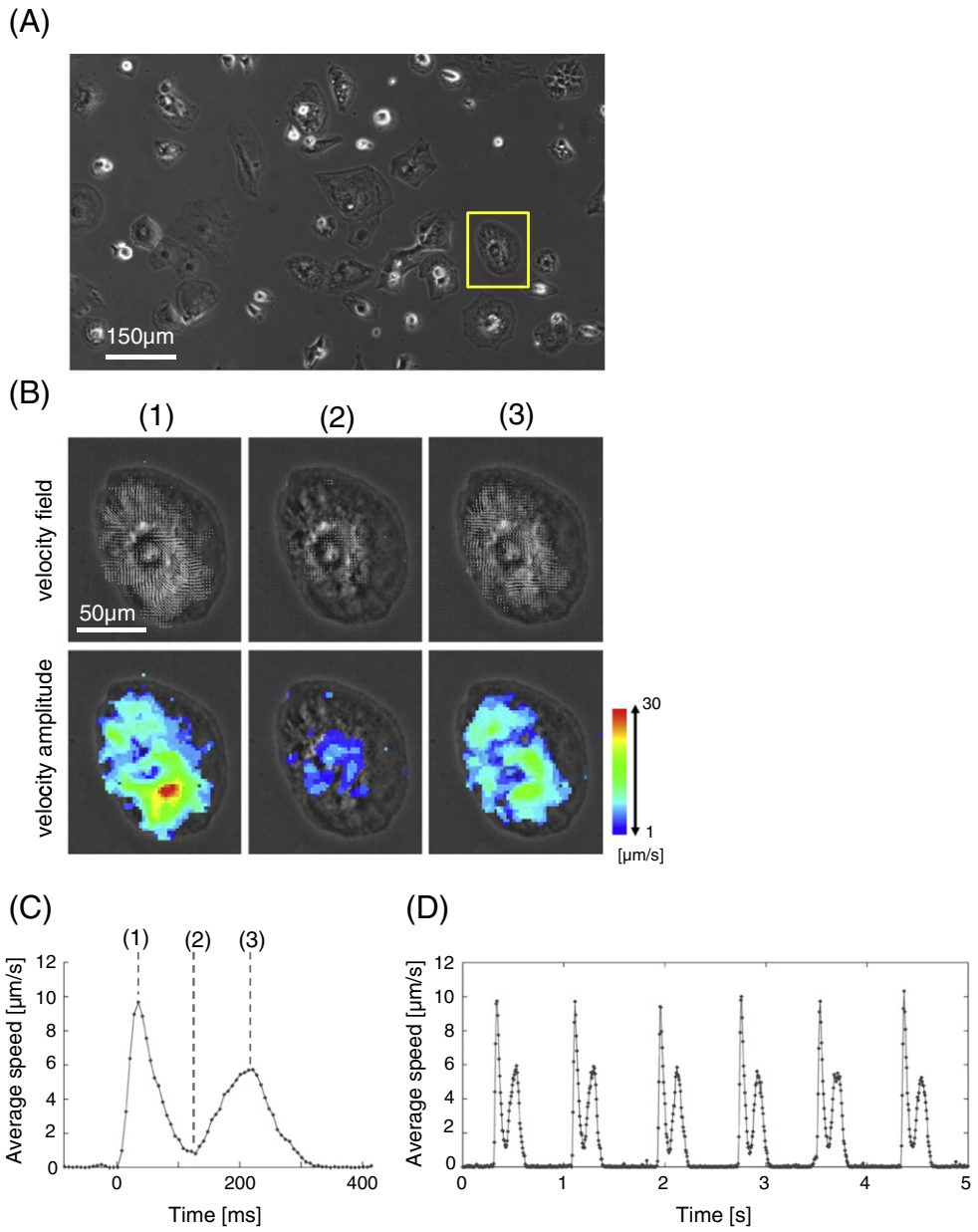

Fig. 1. Motion vectors detected during the contraction and relaxation process of a single hiPS-CM. (A) Example of a phase-contrast image of sparsely plated hiPS-CMs on a collagen-coated polystyrene dish, which was captured using a 10× objective. (B) Contractile motion of the hiPS-CM in the yellow-squared region in (A) was detected using motion vector analysis. In the upper panels, motion vectors show the velocity field at contraction (1), at the end of contraction (2) and at the relaxation (3). Bottom panels show the visualized amplitude of the velocity field in a heat-map style that corresponds to the upper panels. (C) Example of a motion waveform representing contraction and relaxation peaks, calculated with the single hiPS-CM shown in (B). Points (1)–(3) correspond to the same time points in the picture in part (B). (D) The train of motion waveform calculated with the single hiPS-CM shown in (B). (E) Schematics of a motion waveform of CM contraction–relaxation obtained with motion vector analysis. a–c in (E) represent contractile parameters evaluated in the present study, a: maximum contraction speed (MCS), b: maximum relaxation speed (MRS), c: average deformation distance (ADD) and d: contraction–relaxation duration (CRD). (F)–(J) show the summaries of contractile parameters and cell-area of single hiPS-CMs ($n = 40$), evaluated with motion vector analysis. Bars in (F)–(J) represent the average values for each plot. (K) Cell-area dependence of maximum contraction and relaxation speed (MCS and MRS). MCS and MRS were assessed from single hiPS-CMs ($n = 40$) and were plotted against their 2D area. Solid and dotted lines represent linear regression for MCS (black dots) and MRS (gray dots), respectively. (L) Correlation between CRD and the beating rate of single hiPS-CMs ($n = 40$).

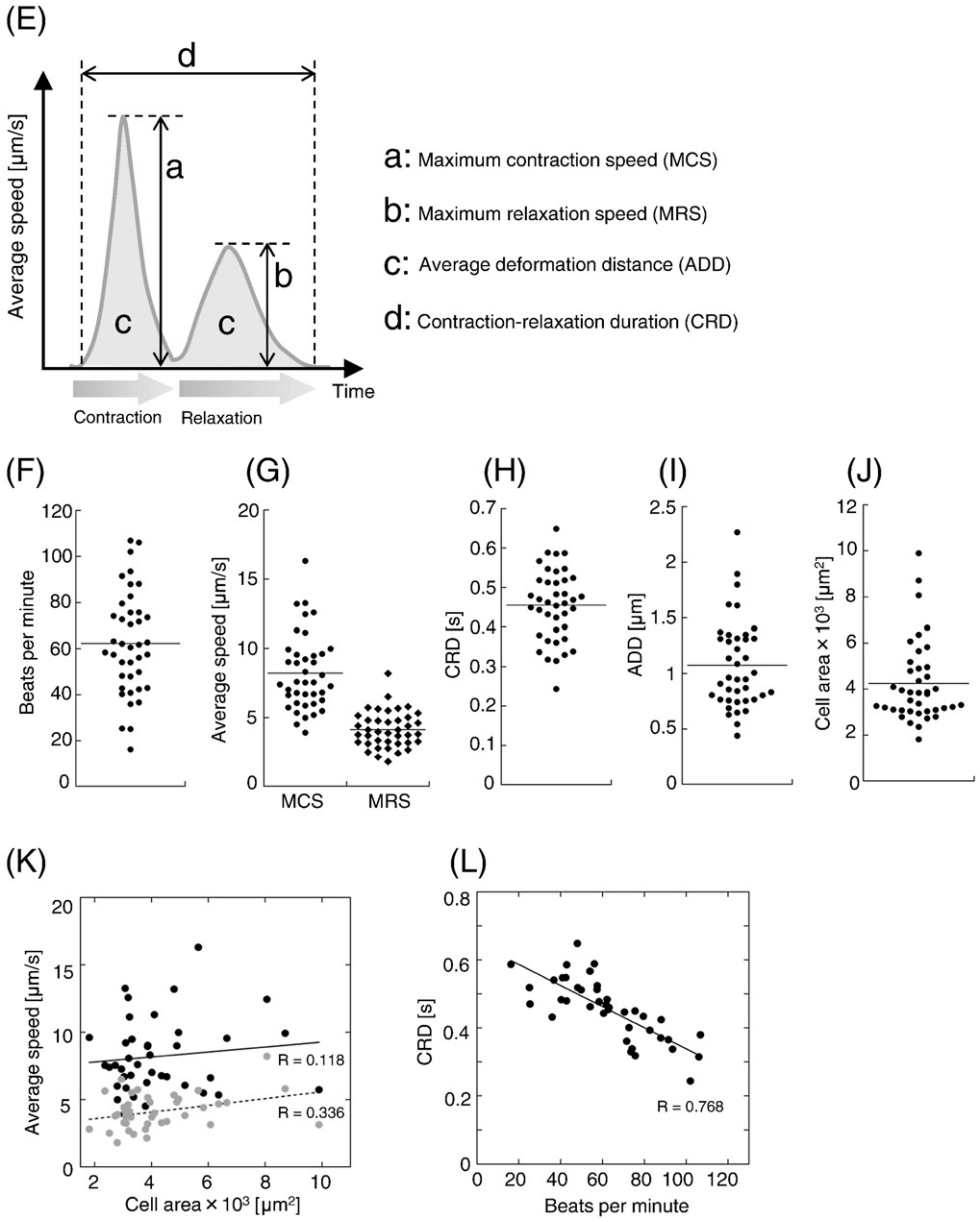

Fig. 1 (*continued*).

cultures [55,58,61]. To confirm the correspondence of these effects on the contractile behaviors of hiPS-CMs, we simultaneously recorded FP and motion of hiPS-CMs in the presence of 0–30 μM of TTX (Fig. 5A). Enlargement of the onset region of Fig. 5A is shown in Fig. 5B. The FP duration from the onset of the positive spike to the peak of the negative spike was significantly prolonged to 161% and 212% of the control at 9 and 30 μM of TTX, respectively, while the FPD measured as the duration between the initial negative peak and the peak of positive deflection increased to 106% and 110% of the control at the same concentrations. Along with the delay of the spikes, the Na^+ peak of FP exhibited broadening and a decrease in the peak slope. The contraction motion also exhibited a delay in the onset and peak position. As shown in Fig. 5C, the durations from the onset of the positive FP spike to the peak of the negative FP spike were linearly correlated with the durations from the onset of the positive FP spike to the onset of the contraction motion peak ($R = 0.856$). Although there was a progressive decrease in the beating rate in accordance with increasing TTX concentrations (Fig. 5G), no major increases in the FPD or CRD were observed (Fig. 5D and G). While the MRS was nearly unaffected, there was a significant decrease in the MCS (Fig. 5E). Despite this major decrease in the MCS, there was no significant alteration in the ADD (Fig. 5F).

3.3.2. The effects of a K^+ channel blocker, E-4031

A K^+ channel (I_{Kr}) blocker, E-4031, prolonged FPD of hiPS-CMs depending on the concentration (Fig. 6A), which is in line with previous reports [54,62]. The motion profile exhibited a prolongation of CRD, with a significant decrease in MRS (Fig. 6A). FPD and CRD showed a linear relationship in the presence of 0–50 nM E-4031 (Fig. 6B) with a correlation coefficient of $R = 0.915$. The slope of the linear regression was 1.362 (FPD/CRD). In the presence of 100 nM E-4031, the hiPS-CMs exhibited an EAD-like FP profile (Fig. 6A and C), i.e., there was an occurrence of negative deflection prior to the positive deflection. Since it was difficult to define the peak point of positive deflection, associated with K^+ current, or FPD in FP waveforms with EAD, we eliminated the data with EAD-like waveform from the evaluation of the CRD–FPD correlation (Fig. 6B). As shown in Fig. 6A and C, the motion profile also exhibited an irregular relaxation pattern that corresponded to the EAD-like FP waveform. This indicates that the speed of the relaxation

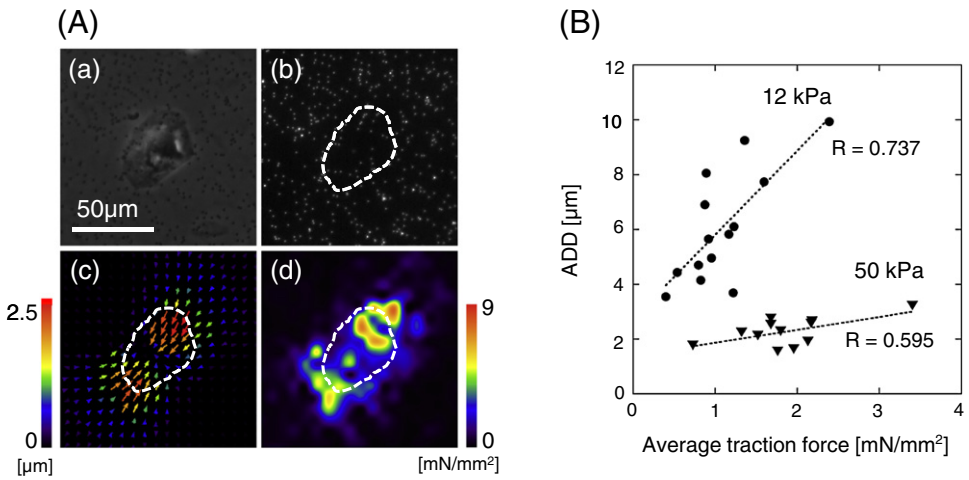

Fig. 2. (A) Parts (a) and (b) show the phase-contrast and fluorescent images of the hiPS-CM and the substrate with fluorescence beads (1 μm diameter), respectively. Part (c) is an example of a displacement field image of fluorescence beads calculated by the particle image velocimetry (PIV) algorithm. Part (d) shows an example of a traction force field image calculated using the PIV result from part (c) by the Fourier transform traction cytometry (FTTC) method. (B) Correlation between ADD and the normalized traction force (at 12 kPa (●) and 50 kPa (▼)) estimated with the FTTC algorithm. Bar in (a) represent 50 μm. The color scales for (c) and (d) are as indicated beside each of the figures.

decreased or almost momentarily stopped at the point of the negative deflection in the FP (see also Supplementary Movies 1 and 2). In the presence of 100 nM E-4031, there was a major decrease in the contractile parameters, MCS, MRS, ADD and the beating rate (Fig. 6E–G).

3.3.3. The effects of a Ca^{2+} channel blocker, verapamil

Fig. 7A shows the alterations in the motion and FP profiles of the hiPS-CMs in accordance with the verapamil concentration (0, 90, 150 nM). Increasing the verapamil concentration caused a progressive decrease in both the FPD and CRD that was well correlated with the correlation coefficient (R = 0.970) (Fig. 7B). The slope of the linear regression was found to be 0.633 (FPD/CRD). Since verapamil has an L-type Ca^{2+}-channel inhibiting effect, increasing verapamil concentration led to a decrease in FP_{slow} (Fig. 7A). Addition of verapamil also caused MCS to become smaller. There was a good correlation between the amplitudes of FP_{slow} and MCS, when these parameters were evaluated as a percent of the control, with a correlation coefficient of 0.921 (Fig. 7C). Increasing verapamil concentration also caused the MRS as well as ADD to decrease (Fig. 7C and D), and the beating rate to increase (Fig. 7E).

3.3.4. The effects of the positive inotropic reagent, isoproterenol

Fig. 8A shows the simultaneously measured motion and FP profile at isoproterenol concentrations of 0, 1, and 10 μM. With increasing isoproterenol concentrations, the CRD and FPD progressively shortened (Fig. 8A), with a good correlation observed (R = 0.943) (Fig. 8B). The slope of the linear regression was found to be 0.737 (FPD/CRD). For the motion profile, there were increases in the MCS, MRS, ADD as well as the beating rate, all depending on isoproterenol concentrations (Fig. 8C and D). These results suggest that the inotropic, lusitropic and chronotropic effects of isoproterenol can be detected with the motion of hiPS-CM monolayer.

3.4. Variability in contractile data

To test the possibility that contractile parameters of hiPS-CMs detected with the motion vector analysis is critically influenced by the heterogeneity in monolayer preparation, we evaluated the regional variability in MCS and MRS. MCS and MRS were obtained from motion data, and are summarized in Supplementary Fig. 3A and B. The average values of MCS and MRS under control conditions varied from 8 to 15 μm/s and from 4 to 10 μm/s, respectively, and were dependent on the regions of monolayer. These values were altered by the addition of a Ca^{2+} channel blocker, verapamil, which had a negative inotropic effect and similar variability to that of the control. By expressing these values to a percent of the control, we found that each value converged to a similar percentage value (Supplementary Fig. 3A and B). This indicates that the relative values of contractile parameters are significantly less dependent on the region in the preparation.

4. Discussion

The present study aimed to evaluate contractile characteristics and the correlation between contractile motion and electrical properties of hiPS-CM monolayer by using video microscopy, Ca^{2+} transient imaging, traction force microscopy and FP measurement. High resolution motion vector analysis could detect contractile characteristics of hiPS-CMs, i.e., MCS, MRS, ADD and CRD, quantitatively, and demonstrated the correspondence between contractile motion and FP. Motion data further provided complementary information against FP, by detecting the inotropic and lusitropic effects of an experimental drug, isoproterenol. The accessibility to information about relaxation process, or lusitropism, is considered to be one of the advantages of this imaging approach. Recently, there has been increasing attention to the diastolic dysfunction characterized by decreased relaxation velocity and prolonged relaxation and its applicability to common cardiac pathologies, such as ischemic heart diseases and hypertensive heart diseases, and to rare genetic heart diseases, such as DCM [63,64]. The imaging approach could potentially be used to target and analyze hiPS-CMs derived from such diseases.

4.1. Contractile characteristics of hiPS-CMs detected with video microscopy

It has been previously reported that alterations in hiPS-CM area depend on substrate stiffness [26] or cell density [65]. We examined the cell area and the contractile parameters (MCS and MRS) of hiPS-CMs ($n = 40$) and observed no significant dependence of MCS and MRS on cell area. Since in our current study, we sparsely plated hiPS-CMs in order to extract single cell information, average cell area became relatively larger (4244 ± 279 μm^2, $n = 40$) than that recently reported (1654 μm^2, $n = 22$) for hiPS-CMs (iCell CMs) that were plated in a monolayer form with a density of 22,500 cells in the well of a 96-well multiplate [65]. As seen in Fig. 1, the hiPS-CMs attached to the substrate exhibited a heterogeneous shape and their contractile motion often

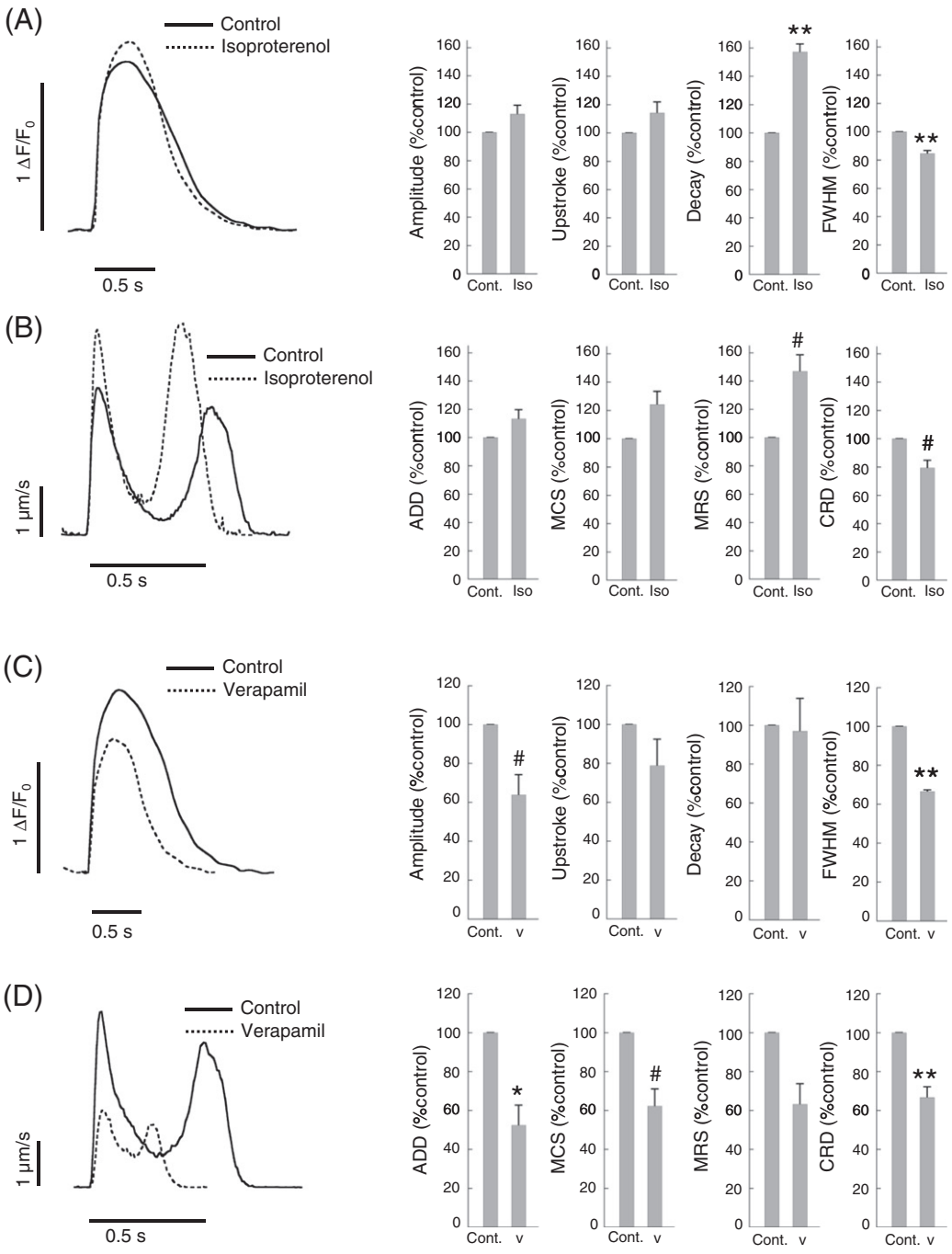

Fig. 3. (A) and (B) show the example profiles of the Ca^{2+} transient and motion waveform of hiPS-CMs, respectively, in the presence of 100 nM isoproterenol. (C) and (D) also show the example profiles of the Ca^{2+} transient and motion waveform of hiPS-CMs, respectively, in the presence of 100 nM verapamil. The bar charts in (A) and (C) represent the drug-induced change in amplitude, maximum upstroke, maximum decay and FWHM of the Ca^{2+}-transient. In (B) and (D), change rate of the contractile parameters, ADD, MCS, MRS and CRD, were also shown in bar charts. The Ca^{2+} transient and motion data were obtained independently. In all the bar charts, values are means ± SE and are expressed as percentage of control.

occurred locally in the cell body. Therefore, it should not be surprising that the average velocity of hiPS-CMs would not correlate well with their cell area. It has been reported that hiPS-CMs cultured for prolonged period, e.g., 90 days, exhibited rod-shaped morphology [66] like adult CMs filled with an aligned sarcomere structure [67]. Those morphologically matured hiPS-CMs, which were not tested in this study, could represent area dependence of contractile speed.

The image-based edge-detection technique has been the method of choice for measuring the shortening of the length of the whole cell body or sarcomere of the rod-shaped adult CMs in order to estimate the force development [34,41–43]. In contrast, TFM has been utilized to assess the contractility of cultured CMs that exhibit an amorphous shape [26,68,69]. With TFM, the traction force of the cells can be estimated based on the deformation of the substrate, which is detected by the displacement of fluorescent beads embedded in the substrate, and on the elastic modulus of the substrate [70]. In our study, we examined the correlation between the force development and cellular deformation (ADD) of the hiPS-CMs. As shown in Fig. 2B, ADD appeared to be correlated with the force development on the substrates (12 kPa and 50 kPa). Phase-contrast microscopy observes

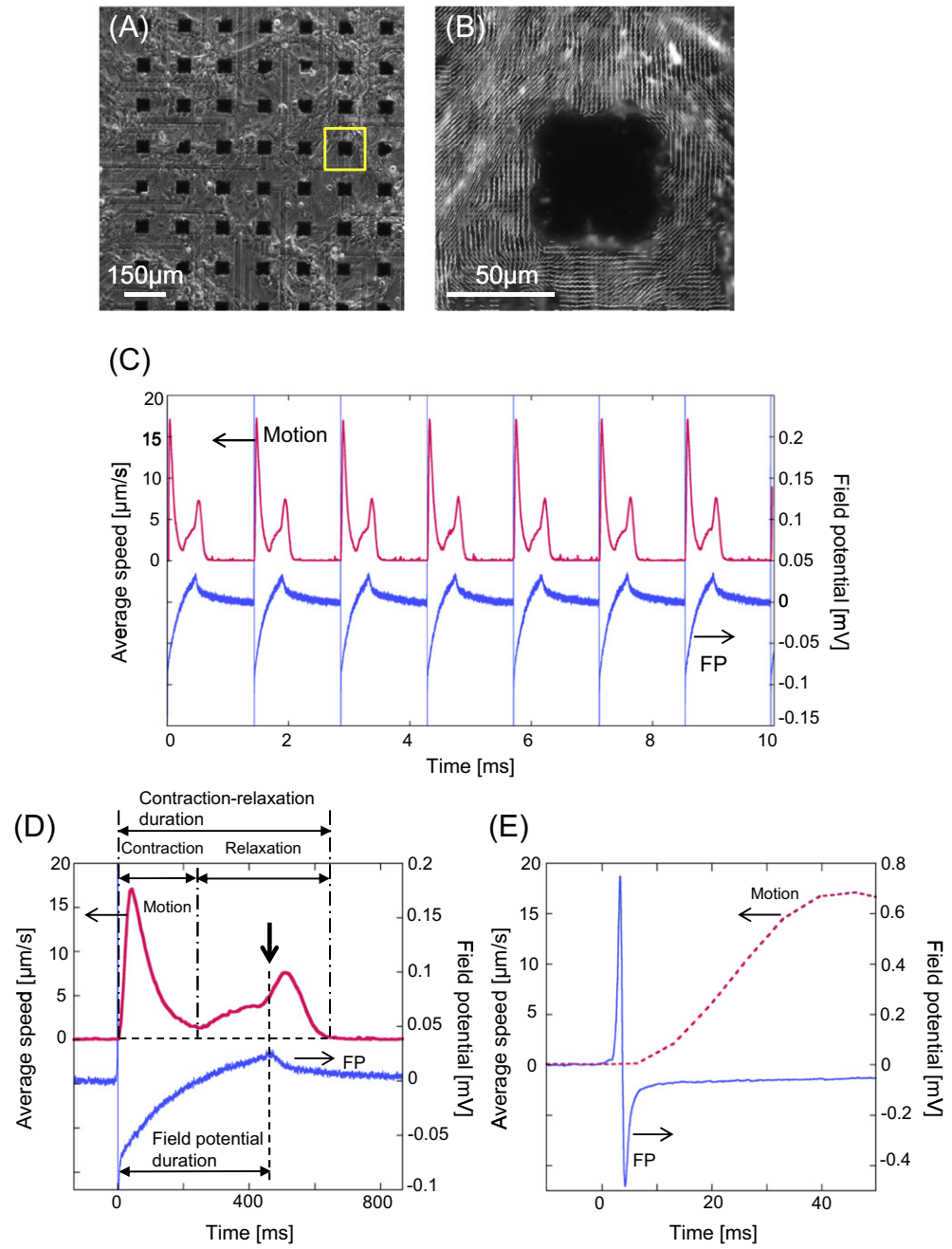

Fig. 4. (A) Phase-contrast image of the hiPS-CM monolayer prepared on the MEA probe. (B) The enlarged velocity field image for the yellow-square region is shown in (A), which shows the motion vectors as fine white lines. (C) Example profile of simultaneously measured hiPS-CM motion and FP. The motion data were evaluated from the region in close vicinity to the electrode (e.g., the yellow-square region in Fig. 4A) that was used for the FP data acquisition. (D) An enlarged single beat profile. The horizontal dashed line represents the baseline of the average velocity (0 μm/s). The vertical dot–dashed lines illustrate the durations of contraction and relaxation of the motion profile. The vertical dashed line with the arrow shows the peak position of positive deflection of the FP. (E) Magnified figure of the onset region of the FP and the motion shown in (D). Time zero corresponds to the onset of the positive FP spike.

overall deformation/displacement of hiPS-CMs during the contraction–relaxation process, including passively moving cellular boundaries and intracellular compartments or organelle. Our present results suggested that the average cellular deformation, ADD, detected by phase-contrast microscopy and motion vector analysis represents the extent of the force development of the hiPS-CMs on the substrates. As long as intra- and extra-cellular elastic properties (e.g., adhesion between hiPS-CMs and substrate) of hiPS-CMs are not altered during the measurement, ADD can be a surrogate marker for the force development of hiPS-CMs.

Isoproterenol and verapamil have been shown to alter the amplitude of the fluorescence peak of the Ca^{2+} transient in iPS-CMs [19]. In our current study, we examined whether the Ca^{2+} transient of hiPS-CMs was correlated with motion behavior in the presence of isoproterenol and verapamil. Responses of the Ca^{2+} transient in hiPS-CMs observed against isoproterenol included an increase in the amplitude, upstroke and decay (Fig. 3A). Interestingly, the maximum decay of the Ca^{2+} transient in the presence of isoproterenol showed a higher increased rate (~160% increase from control) compared to that of maximum upstroke, which is consistent with greater increases in MRS than in MCS of motion

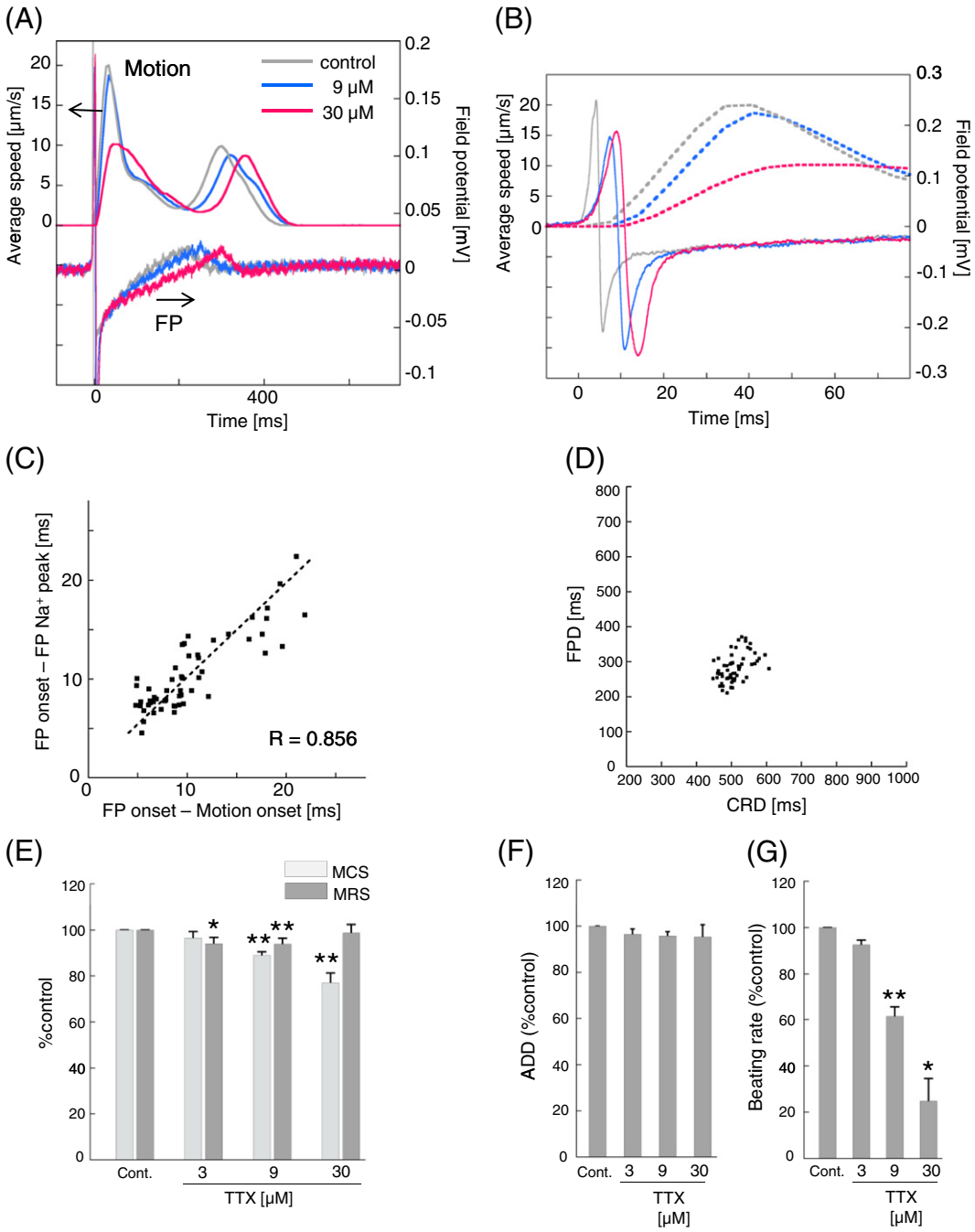

Fig. 5. Contractile and FP responses of the hiPS-CM to tetrodotoxin (TTX). (A) Example of motion and FP profiles of the hiPS-CMs simultaneously measured in the presence of 0, 9, and 30 μM of TTX. (B) Correlation between the CRD and FPD obtained with varied concentrations of TTX (0–30 μM). (C) Enlargement of the onset region of the FP and motion profiles. (D) Correlation of the FP onset-to-FP Na + peak and FP onset-to-motion onset with varied concentrations of TTX (0–30 μM). (E) The normalized change of the MCS and MRS with 0–30 μM of TTX. (F) and (G) show the normalized change of the ADD and beating rate in accordance with the 0–30 μM TTX concentration, respectively. Data were obtained from 15 electrodes with 3 independent preparations and are expressed as means ± SE. $^{*}p < 0.05$; $^{**}p < 0.01$ and $^{\#}p < 0.10$ compared with the control.

response. Verapamil decreased all of the parameters of the Ca^{2+} transient in hiPS-CMs (Fig. 3C, D). This is attributed to verapamil's blockage of the L-type Ca^{2+} channel, which is supported by the FP data shown in Fig. 7C. Thus, decreased contraction and relaxation speeds as well as ADD of hiPS-CMs in the presence of verapamil (Fig. 7D and E) can also be attributed to decreased cytoplasmic Ca^{2+} concentration associated with the Ca^{2+}-induced Ca^{2+} release mechanism. Taken together, these data suggest that the cellular deformation in the hiPS-CM monolayer shows a correspondence to the cytoplasmic Ca^{2+} status, observed with a common fluorescence indicator.

4.2. Correlation between the FP and contractile motion of the hiPS-CMs

Our simultaneous measurements of motion and FP confirmed the following correlations under non-arrhythmic conditions: 1) CRD is longer than the FPD; 2) the onset of contraction motion follows the

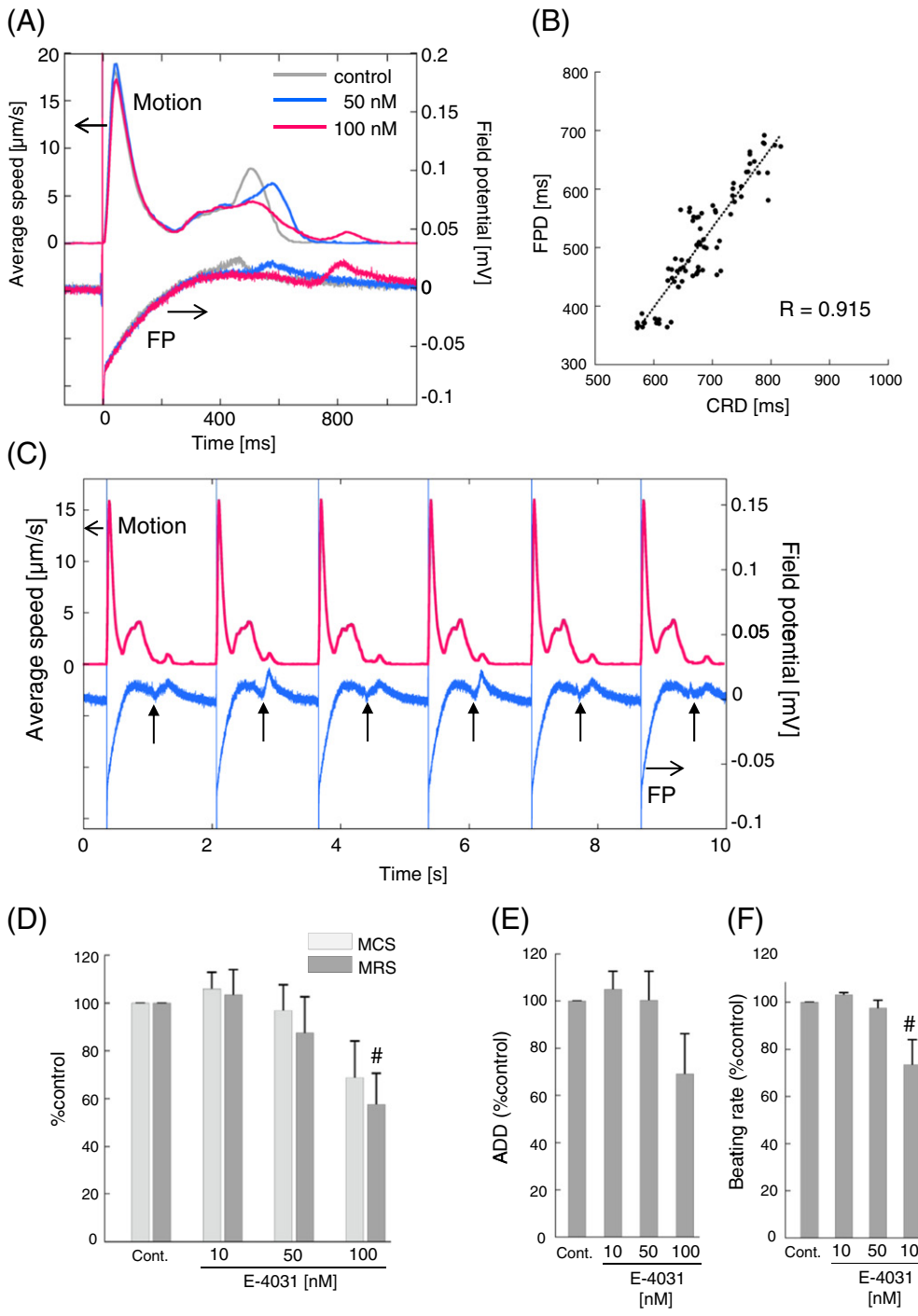

Fig. 6. Contractile and FP responses of the hiPS-CM to E-4031. (A) Example of the motion and FP profiles of the hiPS-CMs simultaneously measured in the presence of 0, 50, and 100 nM of E-4031. (B) Correlation of the CRD and FPD obtained when using varied concentrations of E-4031 (0–~50 nM). Dotted line is a linear regression fitted to the data with R = 0.915 and the slope = 1.362 (FPD/CRD). (C) Relationship between the motion and FP in the presence of 100 nM E-4031. Arrows in (C) indicate the points of the negative deflection in the FP waveform during the relaxation process. Pauses in the relaxation motion corresponded to the negative FP deflections (see also Supplementary Movie 2). (D) Normalized change of the MCS and MRS with 0–100 nM of E-4031. (E) and (F) show the normalized change of the ADD and beating rate in accordance with the 0–100 nM E-4031 concentration changes. Data were obtained from 7 independent preparations of the hiPS-CM monolayer. In (D)–(F), values are expressed as means ± SE. $^{*}p < 0.05$; $^{**}p < 0.01$ and $^{\#}p < 0.10$ compared with the control.

occurrence of the Na^{+} current peak of FP; and 3) the position of the negative broad deflection in FP occurs with the contraction. We also observed relationships 1) and 2), but not 3), in neonatal rat CMs. It is noteworthy that while we found the motion profile of hiPS-CMs exhibited a certain amount of displacement (velocity) at the minimum point between contraction and relaxation peak (Figs. 1 and 4), neonatal rat CMs showed almost no displacement (velocity) at the same position (Supplementary Fig. 2). While this observation for the hiPS-CMs appeared to be derived from the lack of any synchronized motion at the end of the contraction, the precise mechanism for this phenomenon remains unclear. Differences in the contraction motion between hiPS-CMs and rat CMs may reflect the presence and absence of the plateau phase

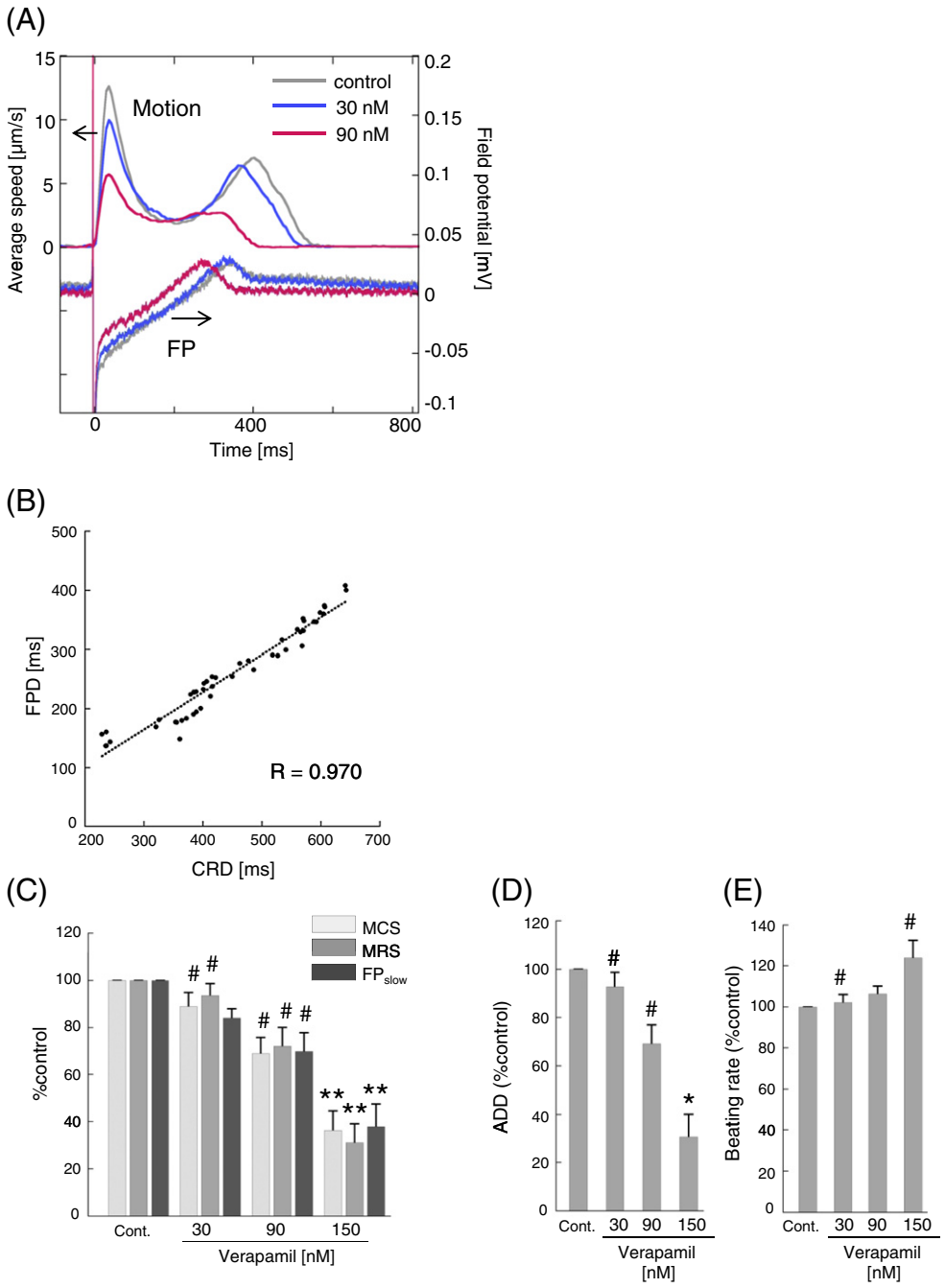

Fig. 7. Contractile and FP responses of the hiPS-CM to verapamil. (A) Example of the motion and FP profiles of the hiPS-CMs simultaneously measured in the presence of 0, 90, and 150 nM of verapamil. (B) Correlation of the CRD and FPD obtained with varied concentrations of verapamil (0–270 nM). Dotted line is a linear regression fitted to the data with R = 0.970 and the slope = 0.633 (FPD/CRD). (C) Change of the rate of the MCS, MRS and the amplitude of FP_{slow}. The amplitude of FP_{slow} was evaluated by averaging the FP value for 6 ms (between 3 ms before and 3 ms after the point of the peak of the contraction motion). (E) and (F) show the normalized change of ADD and beating rate, respectively. Data were obtained from 5 to 8 independent preparations of the hiPS-CM monolayer. In (C)–(E), values are expressed as means ± SE. $^{*}p < 0.05$; $^{**}p < 0.01$ and $^{\#}p < 0.10$ compared with the control.

of their action potential [71–73]. Alternatively, it may be relevant to the immaturity of hiPS-CM sarcoplasmic reticulum, as suggested for hES-CMs [28,29].

We performed a simultaneous measurement of motion and FP from the hiPS-CM monolayer in the presence of TTX, E-4031, verapamil and isoproterenol. The experiments revealed a linear relationship between the CRD and FPD in the presence of E-4031 (10–50 nM), verapamil (30–150 nM) and isoproterenol (0.1–10 μM). Although the slope of the CRD–FPD relationship was suggested to be different in each drug, the present results suggested that the CRD can be a surrogate of the FPD in non-arrhythmic conditions. However, it should be noted that the lower time resolution of motion vector (~6 ms data interval) compared to that of FP (0.05 ms data interval) could be of concern.

Due to the blockage of I_{Kr} with E-4031, it is reasonable to assume that the relaxation speed was decreased at the point where the K^+ current occurred. With regard to the duration, even in the presence of 10–50 nM E-4031, the profile of CRD–FPD correlation appeared to be well correlated with the correlation coefficient of R = 0.915, and the slope of the linear regression was 1.362 (FPD/CRD) (Fig. 6B). This slope value appeared to be significantly larger than the case of verapamil (0.633 (FPD/CRD)) shown in Fig. 7B. This may be relevant to the abnormalities in electro-mechanical relationship reported for the Torsade

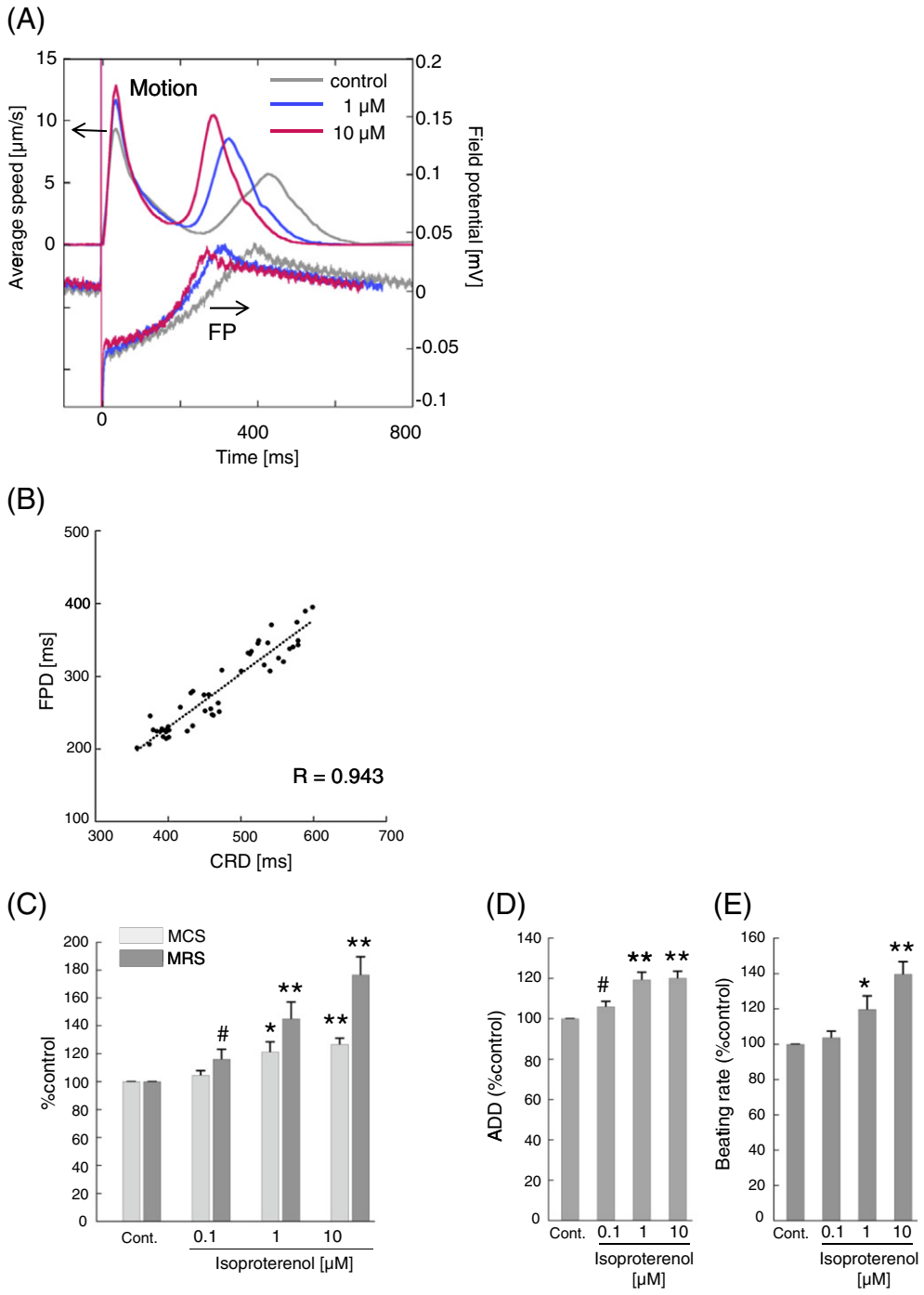

Fig. 8. Contractile and FP responses of the hiPS-CM to isoproterenol. (A) Example of the motion and FP profiles of the hiPS-CMs simultaneously measured in the presence of 0, 1, and 10 μM of isoproterenol. (B) Correlation of the CRD and FPD obtained when using various concentrations of isoproterenol (0–10 μM). Dotted line is a linear regression fitted to the data with R = 0.943 and the slope = 0.738 (FPD/CRD). (C) Normalized change of the MCS and MRS with 0–10 μM of isoproterenol. (D) and (E) show the normalized change of the ADD and beating rate, respectively. Data were evaluated from 7 independent preparations of the hiPS-CM monolayer. In (C)–(E), values are expressed as means ± SE. $^{*}p < 0.05$; $^{**}p < 0.01$ and $^{\#}p < 0.10$ compared with the control.

de Pointes-genic drugs [74–76]. However, to determine the precise relation between FPD and CRD, it is necessary to determine FPD accurately even when the extensive broadening occurred and to consider the beating rate, which is beyond the scope of the present paper and is needed to be examined in a further study. In the presence of 50–100 nM E-4031, the EAD-like negative deflection in the FP waveform was observed. EADs are caused by the re-activation of the inactivated L-type Ca^{2+} current or the inactivated voltage-dependent Na^{+} current, with the latter associated with the activation of the forward cycle of the Na^{+}/Ca^{2+} exchanger and the resultant Ca^{2+} influx. Thus, it is conceivable that the EAD is associated with the transient increase in the intracellular Ca^{2+} concentration, which leads to a reduction of the relaxation motion speed before completion of the relaxation process, thereby resulting in the appearance of another motion peak at the end of relaxation (Fig. 6C). As recognized in the video images of hiPS-CMs in the presence of 100 nM E-4031 (Supplementary video 2), however, such additional single peaks were a part of relaxation motion, not of an independent contraction–relaxation motion. After the occurrence of this type of two-step relaxation motion, triggered activity followed by arrhythmic beating were often observed (data not

shown). EAD-induced contraction, or triggered activity, was also reported using a video edge-detection system for hiPS-CMs in the presence of E-4031 [77]. The occurrence of another motion peak at the end of relaxation could be a potential marker for the early detection of EAD.

Verapamil increased the beating rate of hiPS-CM (Fig. 7E). Although this effect would not be expected to occur based on verapamil's mechanism of action and previous clinical findings [78–80], verapamil has been reported to have a positive chronotropic effect on hES-CMs [54]. In accordance with the concentration of verapamil used in the current study, decreases were observed in MCS and in the amplitude of FP_{slow}. FP_{slow} was also decreased under Ca^{2+}-free condition in embryonic mouse CMs and was suggested to reflect the current of L-type Ca^{2+} channel [55]. Although FP_{slow} does not solely represent the extent of the Ca^{2+} current, their relative values (% of control) were in good agreement with those of the MCS.

Isoproterenol was also observed to increase beating rate, MCS, MRS and ADD. The increasing rate of maximum velocity was greater during relaxation (176% at 10 μM, $n = 7$) versus that during contraction (126% at 10 μM, $n = 7$) (Fig. 8C). Although the precise reason for these findings is currently unknown, Turnbull et al. described the negligible inotropic response of hES-CMs against isoproterenol and pointed out the immaturity of the sarcoplasmic reticulum of the hES-CMs [29]. Pillekampt et al. also reported that isoproterenol significantly induced positive chronotropy and lusitropy but not inotropy in early hES-CMs [28]. The mechanism underlying the hES-CMs findings in their study could be relevant to our current hiPS-CM observations. On the other hand, the FP profile showed no major alterations by the addition of isoproterenol with the exception of the shortening in FPD. Although the L-type Ca^{2+} channel is one of the targets of the isoproterenol action, alterations in FP_{slow} were not clearly detected with isoproterenol. This could be partly due to that negative deflection in FP does not solely reflect the L-type Ca^{2+} current, since the FP is an extracellular potential and not a cell membrane potential.

4.3. Variability in the contractile data

To some extent, the absolute values of MCS and MRS of hiPS-CMs depend on the monolayer region (Supplementary Fig. 3A). The reasons for this regional heterogeneity can be considered to be as follows: 1) the cell density may not be thoroughly homogeneous in the well, 2) the cell size and contractile characteristics have some variability, 3) the hiPS-CM monolayer contains a certain amount of non-cardiac (non-contracting) cells (~2%), and 4) the monolayer preparations contain a variety of shapes and types (atrial-, ventricular- and nodal-type) of hiPS-CMs. However, as long as we evaluate the contractile parameters from the same field of view in the monolayer and express the parameters using a relative value (i.e., % of the control), the inter-region variability of the contractile parameters should be fairly small (Supplementary Fig. 3B). It is possible that non-cardiac cells may have affected the contractile properties of our cultures because those cells move passively with lower motion speed than that of contracting hiPS-CMs. However, we assumed that they were present to a similar extent in all regions in the monolayer and hence should not have affected the validity of our results.

In conclusion, this study demonstrated that the contractile motion of 2D cultured hiPS-CMs, detected by a high-speed camera and motion vector analysis, quantitatively corresponded to their electrophysiological and functional behaviors under non-arrhythmic condition. Although the relationship between hiPS-CM motion and FP during excitation–contraction decoupling or proarrhythmic conditions is of great interest, it is not within the scope of this current paper and will need to be examined in a further study. The results of the present study will open up the possibilities of detecting cellular-level information on the electric and mechanical relationship of cultured CMs and will contribute to expand the applicability of hiPS-CMs in the field of cellular cardiology, drug screening and cardiac therapeutics.

Supplementary data to this article can be found online at http://dx.doi.org/10.1016/j.yjmcc.2014.09.010.

Disclosure Statement

T.H., T.K., S.K., E.M. and H.Y. are employed by Sony Corporation.

References

[1] Habib M, Caspi O, Gepstein L. Human embryonic stem cells for cardiomyogenesis. J Mol Cell Cardiol Oct 2008;45(4):462–74.
[2] Caspi O, Itzhaki I, Kehat I, Gepstein A, Arbel G, Huber I, et al. In vitro electrophysiological drug testing using human embryonic stem cell derived cardiomyocytes. Stem Cells Dev Jan–Feb 2009;18(1):161–72.
[3] Tanaka T, Tohyama S, Murata M, Nomura F, Kaneko T, Chen H, et al. In vitro pharmacologic testing using human induced pluripotent stem cell-derived cardiomyocytes. Biochem Biophys Res Commun Aug 7 2009;385(4):497–502.
[4] Guo L, Abrams RM, Babiarz JE, Cohen JD, Kameoka S, Sanders MJ, et al. Estimating the risk of drug-induced proarrhythmia using human induced pluripotent stem cell-derived cardiomyocytes. Toxicol Sci Sep 2011;123(1):281–9.
[5] Kadota S, Minami I, Morone N, Heuser JE, Agladze K, Nakatsuji N. Development of a reentrant arrhythmia model in human pluripotent stem cell-derived cardiac cell sheets. Eur Heart J Apr 2013;34(15):1147–56.
[6] Nakamura Y, Matsuo J, Miyamoto N, Ojima A, Ando K, Kanda Y, et al. Assessment of testing methods for drug-induced repolarization delay and arrhythmias in an iPS cell-derived cardiomyocyte sheet: multi-site validation study. J Pharmacol Sci 2014;124(4):494–501.
[7] Caspi O, Lesman A, Basevitch Y, Gepstein A, Arbel G, Habib IH, et al. Tissue engineering of vascularized cardiac muscle from human embryonic stem cells. Circ Res Feb 2 2007;100(2):263–72.
[8] Yoshida Y, Yamanaka S. iPS cells: a source of cardiac regeneration. J Mol Cell Cardiol Feb 2011;50(2):327–32.
[9] Kawamura M, Miyagawa S, Fukushima S, Saito A, Miki K, Ito E, et al. Enhanced survival of transplanted human induced pluripotent stem cell-derived cardiomyocytes by the combination of cell sheets with the pedicled omental flap technique in a porcine heart. Circulation Sep 10 2013;128(11 Suppl. 1):S87–94.
[10] Sawa Y, Miyagawa S. Present and future perspectives on cell sheet-based myocardial regeneration therapy. BioMed Res Int 2013;2013:583912.
[11] Matsuura K, Haraguchi Y, Shimizu T, Okano T. Cell sheet transplantation for heart tissue repair. J Control Release Aug 10 2013;169(3):336–40.
[12] Itzhaki I, Schiller J, Beyar R, Satin J, Gepstein L. Calcium handling in embryonic stem cell-derived cardiac myocytes: of mice and men. Ann N Y Acad Sci Oct 2006;1080:207–15.
[13] Satin J, Itzhaki I, Rapoport S, Schroder EA, Izu L, Arbel G, et al. Calcium handling in human embryonic stem cell-derived cardiomyocytes. Stem Cells Aug 2008;26(8):1961–72.
[14] Zwi L, Caspi O, Arbel G, Huber I, Gepstein A, Park IH, et al. Cardiomyocyte differentiation of human induced pluripotent stem cells. Circulation Oct 13 2009;120(15):1513–23.
[15] Itzhaki I, Rapoport S, Huber I, Mizrahi I, Zwi-Dantsis L, Arbel G, et al. Calcium handling in human induced pluripotent stem cell derived cardiomyocytes. PLoS One 2011;6(4):e18037.
[16] Lee YK, Ng KM, Lai WH, Chan YC, Lau YM, Lian Q, et al. Calcium homeostasis in human induced pluripotent stem cell-derived cardiomyocytes. Stem Cell Rev Nov 2011;7(4):976–86.
[17] Jonsson MK, Vos MA, Mirams GR, Duker G, Sartipy P, de Boer TP, et al. Application of human stem cell-derived cardiomyocytes in safety pharmacology requires caution beyond hERG. J Mol Cell Cardiol May 2012;52(5):998–1008.
[18] Zhang GQ, Wei H, Lu J, Wong P, Shim W. Identification and characterization of calcium sparks in cardiomyocytes derived from human induced pluripotent stem cells. PLoS One 2013;8(2):e55266.
[19] Sirenko O, Crittenden C, Callamaras N, Hesley J, Chen YW, Funes C, et al. Multiparameter in vitro assessment of compound effects on cardiomyocyte physiology using iPSC cells. J Biomol Screen Jan 2013;18(1):39–53.
[20] Navarrete EG, Liang P, Lan F, Sanchez-Freire V, Simmons C, Gong T, et al. Screening drug-induced arrhythmia events using human induced pluripotent stem cell-derived cardiomyocytes and low-impedance microelectrode arrays. Circulation Sep 10 2013;128(11 Suppl. 1):S3–S13.
[21] Xi J, Khalil M, Shishechian N, Hannes T, Pfannkuche K, Liang H, et al. Comparison of contractile behavior of native murine ventricular tissue and cardiomyocytes derived from embryonic or induced pluripotent stem cells. FASEB J Aug 2010;24(8):2739–51.
[22] Hansen A, Eder A, Bonstrup M, Flato M, Mewe M, Schaaf S, et al. Development of a drug screening platform based on engineered heart tissue. Circ Res Jul 9 2010;107(1):35–44.
[23] Liau B, Christoforou N, Leong KW, Bursac N. Pluripotent stem cell-derived cardiac tissue patch with advanced structure and function. Biomaterials Dec 2011;32(35):9180–7.
[24] Schaaf S, Shibamiya A, Mewe M, Eder A, Stohr A, Hirt MN, et al. Human engineered heart tissue as a versatile tool in basic research and preclinical toxicology. PLoS One 2011;6(10):e26397.

[25] Tulloch NL, Muskheli V, Razumova MV, Korte FS, Regnier M, Hauch KD, et al. Growth of engineered human myocardium with mechanical loading and vascular coculture. Circ Res Jun 24 2011;109(1):47–59.
[26] Hazeltine LB, Simmons CS, Salick MR, Lian X, Badur MG, Han W, et al. Effects of substrate mechanics on contractility of cardiomyocytes generated from human pluripotent stem cells. Int J Cell Biol 2012;2012:508294.
[27] Liu J, Sun N, Bruce MA, Wu JC, Butte MJ. Atomic force mechanobiology of pluripotent stem cell-derived cardiomyocytes. PLoS One 2012;7(5):e37559.
[28] Pillekamp F, Haustein M, Khalil M, Emmelheinz M, Nazzal R, Adelmann R, et al. Contractile properties of early human embryonic stem cell-derived cardiomyocytes: beta-adrenergic stimulation induces positive chronotropy and lusitropy but not inotropy. Stem Cells Dev Aug 10 2012;21(12):2111–21.
[29] Turnbull IC, Karakikes I, Serrao GW, Backeris P, Lee JJ, Xie C, et al. Advancing functional engineered cardiac tissues toward a preclinical model of human myocardium. FASEB J Feb 2014;28(2):644–54.
[30] Sun N, Yazawa M, Liu J, Han L, Sanchez-Freire V, Abilez OJ, et al. Patient-specific induced pluripotent stem cells as a model for familial dilated cardiomyopathy. Sci Transl Med Apr 18 2012;4(130):130ra47.
[31] Tameyasu T, Toyoki T, Sugi H. Nonsteady motion in unloaded contractions of single frog cardiac cells. Biophys J Sep 1985;48(3):461–5.
[32] O'Rourke B, Reibel DK, Thomas AP. High-speed digital imaging of cytosolic Ca^{2+} and contraction in single cardiomyocytes. Am J Physiol Jul 1990;259(1 Pt 2):H230–42.
[33] Pollack PS, Carson NL, Nuss HB, Marino TA, Houser SR. Mechanical properties of adult feline ventricular myocytes in culture. Am J Physiol Jan 1991;260(1 Pt 2):H234–41.
[34] Mukherjee R, Crawford FA, Hewett KW, Spinale FG. Cell and sarcomere contractile performance from the same cardiocyte using video microscopy. J Appl Physiol Apr 1993;74(4):2023–33.
[35] Stummann TC, Wronski M, Sobanski T, Kumpfmueller B, Hareng L, Bremer S, et al. Digital movie analysis for quantification of beating frequencies, chronotropic effects, and beating areas in cardiomyocyte cultures. Assay Drug Dev Technol Jun 2008;6(3):375–85.
[36] Kamgoue A, Ohayon J, Usson Y, Riou L, Tracqui P. Quantification of cardiomyocyte contraction based on image correlation analysis. Cytometry A Apr 2009;75(4):298–308.
[37] Bazan C, Barba DT, Blomgren P, Paolini P. Image processing techniques for assessing contractility in isolated adult cardiac myocytes. Int J Biomed imaging 2009;2009:352954.
[38] Bazan C, Torres Barba D, Blomgren P, Paolini P. Image processing techniques for assessing contractility in isolated neonatal cardiac myocytes. Int J Biomed imaging 2011;2011:729732.
[39] Hossain MM, Shimizu E, Saito M, Rao SR, Yamaguchi Y, Tamiya E. Non-invasive characterization of mouse embryonic stem cell derived cardiomyocytes based on the intensity variation in digital beating video. Analyst Jul 2010;135(7):1624–30.
[40] Harmer AR, Abi-Gerges N, Morton MJ, Pullen GF, Valentin JP, Pollard CE. Validation of an in vitro contractility assay using canine ventricular myocytes. Toxicol Appl Pharmacol Apr 15 2012;260(2):162–72.
[41] Harding SE, Vescovo G, Kirby M, Jones SM, Gurden J, Poole-Wilson PA. Contractile responses of isolated adult rat and rabbit cardiac myocytes to isoproterenol and calcium. J Mol Cell Cardiol Jul 1988;20(7):635–47.
[42] Vescovo G, Harding SE, Jones SM, Dalla Libera L, Pessina AC, Poole-Wilson PA. Comparison between isomyosin pattern and contractility of right ventricular myocytes isolated from rats with right cardiac hypertrophy. Basic Res Cardiol Sep–Oct 1989;84(5):536–43.
[43] Steadman BW, Moore KB, Spitzer KW, Bridge JH. A video system for measuring motion in contracting heart cells. IEEE Trans Biomed Eng Apr 1988;35(4):264–72.
[44] He JQ, Ma Y, Lee Y, Thomson JA, Kamp TJ. Human embryonic stem cells develop into multiple types of cardiac myocytes: action potential characterization. Circ Res Jul 11 2003;93(1):32–9.
[45] Brito-Martins M, Harding SE. Ali NN. beta(1)- and beta(2)-adrenoceptor responses in cardiomyocytes derived from human embryonic stem cells: comparison with failing and non-failing adult human heart. Br J Pharmacol Feb 2008;153(4):751–9.
[46] Ahola A, Kiviaho AL, Larsson K, Honkanen M, Aalto-Setala K, Hyttinen J. Video image-based analysis of single human induced pluripotent stem cell derived cardiomyocyte beating dynamics using digital image correlation. Biomed Eng Online 2014;13(1):39.
[47] Hayakawa T, Kunihiro T, Dowaki S, Uno H, Matsui E, Uchida M, et al. Noninvasive evaluation of contractile behavior of cardiomyocyte monolayers based on motion vector analysis. Tissue Eng Part C Methods Jan 2012;18(1):21–32.
[48] Ma J, Guo L, Fiene SJ, Anson BD, Thomson JA, Kamp TJ, et al. High purity human-induced pluripotent stem cell-derived cardiomyocytes: electrophysiological properties of action potentials and ionic currents. Am J Physiol Nov 2011;301(5):H2006–17.
[49] Ghanbari M. The cross-search algorithm for motion estimation. Trans Commun 1990;38(7):950–3.
[50] Dembo M, Wang YL. Stresses at the cell-to-substrate interface during locomotion of fibroblasts. Biophys J Apr 1999;76(4):2307–16.
[51] Sabass B, Gardel ML, Waterman CM, Schwarz US. High resolution traction force microscopy based on experimental and computational advances. Biophys J Jan 1 2008;94(1):207–20.
[52] Tseng Q, Duchemin-Pelletier E, Deshiere A, Balland M, Guillou H, Filhol O, et al. Spatial organization of the extracellular matrix regulates cell–cell junction positioning. Proc Natl Acad Sci U S A Jan 31 2012;109(5):1506–11.
[53] Butler JP, Tolic-Norrelykke IM, Fabry B, Fredberg JJ. Traction fields, moments, and strain energy that cells exert on their surroundings. Am J Physiol Cell Physiol Mar 2002;282(3):C595–605.
[54] Yamazaki K, Hihara T, Taniguchi T, Kohmura N, Yoshinaga T, Ito M, et al. A novel method of selecting human embryonic stem cell-derived cardiomyocyte clusters for assessment of potential to influence QT interval. Toxicol In Vitro Mar 2012;26(2):335–42.
[55] Halbach M, Egert U, Hescheler J, Banach K. Estimation of action potential changes from field potential recordings in multicellular mouse cardiac myocyte cultures. Cell Physiol Biochem 2003;13(5):271–84.
[56] Meyer T, Boven KH, Gunther E, Fejtl M. Micro-electrode arrays in cardiac safety pharmacology: a novel tool to study QT interval prolongation. Drug Saf 2004;27(11):763–72.
[57] Egert U, Meyer T. Heart on a chip — extracellular multielectrode recordings from cardiomyocytes in vitro; 2005.
[58] Reppel M, Igelmund P, Egert U, Juchelka F, Hescheler J, Drobinskaya I. Effect of cardioactive drugs on action potential generation and propagation in embryonic stem cell-derived cardiomyocytes. Cell Physiol Biochem 2007;19(5–6):213–24.
[59] Liang H, Matzkies M, Schunkert H, Tang M, Bonnemeier H, Hescheler J, et al. Human and murine embryonic stem cell-derived cardiomyocytes serve together as a valuable model for drug safety screening. Cell Physiol Biochem 2010;25(4–5):459–66.
[60] Matsa E, Rajamohan D, Dick E, Young L, Mellor I, Staniforth A, et al. Drug evaluation in cardiomyocytes derived from human induced pluripotent stem cells carrying a long QT syndrome type 2 mutation. Eur Heart J Apr 2011;32(8):952–62.
[61] Braam SR, Tertoolen L, van de Stolpe A, Meyer T, Passier R, Mummery CL. Prediction of drug-induced cardiotoxicity using human embryonic stem cell-derived cardiomyocytes. Stem Cell Res Mar 2009;4(2):107–16.
[62] Nomura F, Kaneko T, Hattori A, Yasuda K. On-chip constructive cell-network study (II): on-chip quasi-in vivo cardiac toxicity assay for ventricular tachycardia/fibrillation measurement using ring-shaped closed circuit microelectrode with lined-up cardiomyocyte cell network. J Nanobiotechnol 2011;9:39.
[63] Periasamy M, Bhupathy P, Babu GJ. Regulation of sarcoplasmic reticulum Ca^{2+} ATPase pump expression and its relevance to cardiac muscle physiology and pathology. Cardiovasc Res Jan 15 2008;77(2):265–73.
[64] Borlaug BA, Kass DA. Mechanisms of diastolic dysfunction in heart failure. Trends Cardiovasc Med Nov 2006;16(8):273–9.
[65] Uesugi M, Ojima A, Taniguchi T, Miyamoto N, Sawada K. Low-density plating is sufficient to induce cardiac hypertrophy and electrical remodeling in highly purified human iPS cell-derived cardiomyocytes. J Pharmacol Toxicol Methods 2014;69(2):177–88.
[66] Shinozawa T, Imahashi K, Sawada H, Furukawa H, Takami K. Determination of appropriate stage of human-induced pluripotent stem cell-derived cardiomyocytes for drug screening and pharmacological evaluation in vitro. J Biomol Screen Oct 2012;17(9):1192–203.
[67] Bird SD, Doevendans PA, van Rooijen MA, Brutel de la Riviere A, Hassink RJ, Passier R, et al. The human adult cardiomyocyte phenotype. Cardiovasc Res May 1 2003;58(2):423–34.
[68] Bhana B, Iyer RK, Chen WL, Zhao R, Sider KL, Likhitpanichkul M, et al. Influence of substrate stiffness on the phenotype of heart cells. Biotechnol Bioeng Apr 15 2010;105(6):1148–60.
[69] Hersch N, Wolters B, Dreissen G, Springer R, Kirchgessner N, Merkel R, et al. The constant beat: cardiomyocytes adapt their forces by equal contraction upon environmental stiffening. Biol Open Mar 15 2013;2(3):351–61.
[70] Wang JH, Lin JS. Cell traction force and measurement methods. Biomech Model Mechanobiol Nov 2007;6(6):361–71.
[71] Langer GA, Brady AJ, Tan ST, Serena D. Correlation of the glycoside response, the force staircase, and the action potential configuration in the neonatal rat heart. Circ Res Jun 1975;36(6):744–52.
[72] Zhang J, Wilson GF, Soerens AG, Koonce CH, Yu J, Palecek SP, et al. Functional cardiomyocytes derived from human induced pluripotent stem cells. Circ Res Feb 27 2009;104(4):e30–41.
[73] Honda M, Kiyokawa J, Tabo M, Inoue T. Electrophysiological characterization of cardiomyocytes derived from human induced pluripotent stem cells. J Pharmacol Sci 2011;117(3):149–59.
[74] van der Linde HJ, Van Deuren B, Somers Y, Loenders B, Towart R, Gallacher DJ. The electro-mechanical window: a risk marker for Torsade de Pointes in a canine model of drug induced arrhythmias. Br J Pharmacol Dec 2010;161(7):1444–54.
[75] Guns PJ, Johnson DM, Van Op den Bosch J, Weltens E, Lissens J. The electro-mechanical window in anaesthetized guinea pigs: a new marker in screening for Torsade de Pointes risk. Br J Pharmacol May 2012;166(2):689–701.
[76] Guns PJ, Johnson DM, Weltens E, Lissens J. Negative electro-mechanical windows are required for drug-induced Torsades de Pointes in the anesthetized guinea pig. J Pharmacol Toxicol Methods Sep 2012;66(2):125–34.
[77] Doss MX, Di Diego JM, Goodrow RJ, Wu Y, Cordeiro JM, Nesterenko VV, et al. Maximum diastolic potential of human induced pluripotent stem cell-derived cardiomyocytes depends critically on I(Kr). PLoS One 2012;7(7):e40288.
[78] Wellens HJ, Tan SL, Bar FW, Duren DR, Lie KI, Dohmen HM. Effect of verapamil studied by programmed electrical stimulation of the heart in patients with paroxysmal re-entrant supraventricular tachycardia. Br Heart J Oct 1977;39(10):1058–66.
[79] Gay R, Algeo S, Lee R, Olajos M, Morkin E, Goldman S. Treatment of verapamil toxicity in intact dogs. J Clin Invest Jun 1986;77(6):1805–11.
[80] Nazzaro P, Manzari M, Merlo M, Triggiani R, Scarano AM, Lasciarrea A, et al. Antihypertensive treatment with verapamil and amlodipine. Their effect on the functional autonomic and cardiovascular stress responses. Eur Heart J Sep 1995;16(9):1277–84.